5-17-2016

Spectral Analysis of X-Ray Emission Mechanisms in Local Astrophysical Environments

Bradford T. Snios
University of Connecticut, snios@phys.uconn.edu

Spectral Analysis of X-Ray Emission Mechanisms in Local Astrophysical Environments

Bradford Snios, Ph.D.

University of Connecticut, 2016

In order to establish contributions of different X-ray emission mechanisms from local astrophysical environments, we perform a theoretical analysis of observed cometary X-ray emission spectra. We develop a model from first principles that generates updated spectra of solar wind charge-exchange (CX) emissions together with accurate scattering and fluorescence spectra of solar X-rays by atoms, molecules, and dust/ice particles. This model also explores scattering and fluorescence spectra for different solar conditions, including spectra induced by solar X-ray flares of different classes and durations. We compare the modeled spectra with cometary and planetary observations from the *Chandra X-Ray Observatory* Advanced CCD Imaging Spectrometer (ACIS) and determine the primary emission mechanisms for both the 0.3–1.0 keV and 1.0–2.0 keV photon energy ranges. These comparisons establish upper limits on cometary dust/ice mass production rates and grain size distributions. Our results also demonstrate the utility of charge-exchange emissions as a remote diagnostics tool of both astrophysical

plasma interaction and solar wind composition. In addition, we observe potential soft X-ray emissions via ACIS around 0.2 keV that are correlated in intensity to the hard X-ray emissions between 0.4–1.0 keV. We fit our CX model to these emissions, but our lack of a unique solution at low energies makes it impossible to conclude if they are cometary CX in origin. Finally, we discuss probable emission mechanism sources for these soft X-rays and explore new opportunities these findings present in understanding emission processes via Chandra.

Spectral Analysis of X-Ray Emission Mechanisms in Local Astrophysical Environments

Bradford Snios

B.S., Rochester Institute of Technology, 2009

M.S., University of Connecticut, 2013

A Dissertation

Submitted in Partial Fulfillment of the

Requirements for the Degree of

Doctor of Philosophy

at the

University of Connecticut

2016

APPROVAL PAGE

Doctor of Philosophy Dissertation

Spectral Analysis of X-Ray Emission Mechanisms in Local Astrophysical Environments

Presented by

Bradford Snios, M.S.

Major Advisor

Vasili Kharchenko

Associate Advisor

Robin Côté

Associate Advisor

Phillip Mannheim

University of Connecticut

2016

I dedicate this work to my parents, Barbara and Ronald, who taught me to think like a scientist before I ever knew what a scientist was.

ACKNOWLEDGEMENTS

Looking back at everything required to complete a Ph.D., I realize how grateful I am for those people who supported me every step of the way. I would like to thank my advisor Dr. Vasili Kharchenko for his guidance over the years. For any topic of discussion, Vasili has proven to be a great mentor as well as a great friend. I would also like to thank my co-advisors Dr. Robin Côté and Dr. Phillip Mannheim whose guidance through my dissertation writing has been indispensable. Additionally, I thank Dr. Casey Lisse, Dr. Scott Wolk, Dr. Konrad Dennerl, and Dr. Michael Combi for their collaborative efforts with me and for their invaluable advice. My family has also been the driving force for much of my success, and so I thank my parents Barbara and Ronald Snios who taught me the value of hard work and dedication. I also thank my girlfriend Katya for her constant love and support. Lastly, I would like to thank all my fellow graduate students who have been great friends and were always there to help me unwind after a stressful week.

TABLE OF CONTENTS

LIST OF FIGURES

LIST OF TABLES

Chapter 1

Introduction

Investigation of emissions from astrophysical environments has seen great progress in recent years due to the increase in spaced-based telescopes. Removal of the signal attenuation and extinction caused by the Earth's atmosphere has allowed astronomers to develop a deeper understanding of various astrophysical sources, such as solar wind emissions, stellar formation in distant nebula, and binary black hole evolution. In particular, the study of astrophysical X-ray emissions has rapidly expanded through the introduction of long-exposure, high-resolution X-ray observations that were previously impractical via other observing techniques. It is through the comparison of these observations with accurate physical models of X-ray emissions that we establish a more complete picture of the universe. As such, the study and categorization of X-ray emission mechanisms is a key component to any astrophysical investigation.

Consistently bright X-ray sources are exotic due to the high temperatures required to produce such emissions. Instead, most X-ray sources are variable in intensity and only emit strongly when unusual physical conditions are met. Due to these irregular emission rates and the inverse-squared dependence on distance for these intensities,

it is challenging to detect high photon count rates from most interstellar and intergalactic X-ray sources without long exposure observations, frequent surveys, or abnormally high activity from the host object. This work therefore focuses on the analyses of X-ray emissions from interplanetary bodies, such as planets and comets, as the short detection distance provides higher counts without the necessity for significantly long telescope exposure times. Each selected object is investigated through post-process imaging techniques to obtain an accurate physical emission morphology and emission spectrum, which can be used to explore local conditions as well as emission mechanism sources present within each system.

X-ray emissions from interplanetary objects are dominated by three mechanisms: charge-exchange between neutral atoms and solar wind ions, scattering of solar X-rays, and fluorescence. Each mechanism depends on different physical parameters of the observed systems that dictate the overall emission intensity and spectral shape. In this thesis, emission spectrum models are developed from first principles for each mechanism over the observable X-ray energy range using accurate theoretical and experimental cross section results. Comparison of the modeled spectra to observational data provides valuable insight into the ratios at which these mechanisms operate within different systems and how various physical parameters impact these ratios. In addition, examination of different mechanisms may yield several interesting physical insights, which may include: source object chemical composition, solar wind composition, solar wind speed, interaction region between solar wind and the object, dust particle densi-

ties, dust particle radius dependence, dependence of emission on solar conditions, time variability of emissions, and changes in the detector over time. This makes emission modeling an important process due to the significant amount of new and interesting physics that can be obtained from its analysis.

This work begins with a description of post-processing techniques incorporated to extract physical results from observational data. Afterward, a discussion of modeling X-ray emissions via charge-exchange, scattering, and fluorescence emissions is performed. Finally, modeling results are compared to observations and their implications are analyzed, followed by conclusions.

Chapter 2

Photometric Reductions

Detection of X-ray emissions from astrophysical systems is a significant challenge due to the short penetration depth of X-ray photons into Earth's atmosphere, requiring all X-ray observatories to be high altitude detectors, such as high-altitude balloons or satellites. Even after removing the effects of the atmosphere, intense X-ray emissions are exotic from most astrophysical systems, requiring significant exposure time for the detector to properly resolve any objects. These difficulties result in fewer observatories and lower signal-to-noise ratios than present for other wavelength bands, requiring careful post-processing of images to ensure all critical data is preserved as even the loss of few counts in an image can significantly alter the results. It is therefore crucial that any discussion of astrophysical X-ray observations begin with a thorough analysis of the observatory used and the post-processing techniques employed to ensure statistically and physically relevant results.

2.1 *Chandra* Overview

All observations analyzed in this research were taken by the *Chandra X-Ray Observatory* (*Chandra*). Launched July 23, 1999, *Chandra* is in a high ecliptic orbit around the Earth and possesses a suite of instruments designed to observe X-ray sources through both morphological and spectroscopic analysis. These instruments include the High Resolution Camera (HRC), Advanced CCD Imaging Spectrometer (ACIS), High Energy Transmission Grating Spectrometer (HETGS), and the Low Energy Transmission Grating Spectrometer (LETGS).

Local astrophysical objects have frequently been observed with *Chandra* over the course of the telescope's lifetime [1]. In practice, the HETGS and LETGS instruments have proven to be of little use in such cases due to the distended nature of local objects when viewed. Therefore, all local observations are performed with either ACIS or HRC, and a description of each can be found in Table 2.1 as well as in the following sections.

2.1.1 ACIS Instrument

The ACIS instrument is composed of two CCD arrays comprised of over 10 different chips. The first array is titled ACIS-I and is a 4-chip, 2×2 array used for wide-field images, with a field-of-view of 16'×16', and CCD imaging spectrometry. All chips present in ACIS-I are front-illuminated CCDs, which offers a higher energy response at the cost of a reduced observable energy range. ACIS-I possesses an observable energy

Instrument	Scientific Use	Aimpoint	FOV (arcmin)	Energy Resolution (eV)	Time Resolution (sec)
ACIS-I	Wide-Field Imaging	I3	16.9×16.9	130 @ 1.49 keV	3.2
ACIS-S	Imaging Spectrometry	S3	8.3×50.6	95 @ 1.49 keV	3.2
HRC-I	Wide-Field Imaging	–	30×30	–	–
HRC-S	Timing Mode	–	6×30	–	1.6e-5

Table 2.1: An overview of all *Chandra* instruments frequently utilized for local astrophysical observations. See the *Chandra Proposal Handbook* for further instrument specfications.

range of 0.6–11 keV, with its highest sensitivity at energies greater than 1.0 keV.

The second ACIS array is ACIS-S, and it is a 6-chip, 6×1 array with a 8.3'×50.6' field-of-view used primarily for CCD imaging spectrometry, occasionally in conjunction with the HETGS instrument. ACIS-S is unique in that two of its six chips, S1 and S3, are back-illuminated. Back-illumination means that the insensitive silicon material on the back of the chip has been removed, and the chip is then deployed with the back side facing outward. This is done to reduce the photon penetration depth required for a detection when compared to front-illumination, allowing for back-illuminated chips to achieve a higher sensitivity to lower energy photons. For the back-illuminated chips, ACIS-S can achieve an observable energy range of 0.3–11 keV, with much improved sensitivity towards soft X-rays over what is seen from the front-illuminated chips. Of the two back-illuminated chips present, the S3 chip is primarily used as it resides in the center of the array and possesses a slightly higher sensitivity than S1.

Over its lifespan, the ACIS instrument has shown degradation in its sensitivity, with the 0.3–1.0 keV energy range sensitivity decreasing by a factor of 3 since its initial testing. This degradation is likely due to molecular contamination buildup on the optical blocking filter, an effect that will increase the required photon penetration depth and therefore reduce the soft X-ray detection rates. In addition, radiation damage due to high energy protons reflecting through the telescope early in *Chandra*'s mission has created several dead pixels across the various CCDs. As this work investigates and compares observations taken over the course of *Chandra*'s lifetime, it is important to properly correct for the differences in detector characteristics before performing the analysis. Further details on this topic are discussed in Sect. 2.5.

2.1.2 HRC Instrument

The HRC instrument is comprised of two microchannel plate imaging detectors. The HRC-I is designed for wide-field imaging, while the HRC-S serves as a read-out for the LETGS. As we are concerned with local astrophysical objects and therefore are using the LETGS, we focus our attention on the HRC-I.

The HRC-I possesses the largest field-of-view of any *Chandra* detector (30'×30') and is placed at right angles to the optical axis, tangent to the focal surface. It also possesses the best time resolution of *Chandra* at 16 μsec. In addition, its response extends to energies below the sensitivity of ACIS with an overall energy range of 0.06–10 keV, although it lacks in overall spectral resolution. The lower energy sensitivity

makes HRC-I an excellent complement to ACIS-S observations when analyzing the morphologies and time variance of soft X-ray emissions.

2.2 *Chandra* Observations

All observations analyzed in this research were taken using either ACIS-S of HRC-I. For the ACIS observations, the object was centered on the S3 chip and ACIS was set to very faint mode for all observations. Very faint mode, also called vfaint, outputs the position, time, pulse height, and pixel location for each detected event while also recording telemetry from a 5×5 area of surrounding pixels. Examination of adjacent pixels allows the detector to assist in filtering out bad X-ray events, such as cosmic X-rays, from the source events. This mode is considered standard for observations of diffuse systems, but total intensity from source object must be considered as the additional telemetry reduces ACIS' total saturation threshold. As all of our observations were of X-ray dim objects, we need not worry about detector saturation. All observations were also performed in drift-scan mode where no active guidance is enabled and *Chandra's* pointing was only updated to re-center before the object moved off the chip. This technique is a common practice for local object observations to ensure high exposure times and minimal emission drift due to *Chandra's* movement.

2.3 Image Reproccessing

Since all observations were performed in drift-scan mode, the first step is to convert all images to object-centered coordinates. We may perform this by reprojecting the photon event locations extracted from the observation in conjunction with the mapped trajectory of the object over the exposure duration to produce a new image with object-centered coordinates. For this process, we may use of the *sso_freeze* routine found in the *Chandra* Interactive Analysis of Observations (CIAO) software package, a set of software tools specifically designed to assist in the data processing and analysis of *Chandra* observations [2]. A by-product of this process is non-uniform exposure across the resulting image, which is notable at the image edges that experienced an exposure duration lower than the total observation time due to the motion of the telescope. Exposure map correction must therefore be performed to weight the total counts in each pixel to its exposure time in order to obtain an accurate emission image. Once completed, accurate morphological and spectroscopic analysis of the source object may begin.

When beginning image analysis, the detected photons must be separated between those from the source object currently being studied and those from background emissions coming from distant objects also present in the image. Therefore, clear and distinct source and background regions must be selected for each image. Source regions are designated as those pixels dominated by emission from the source objects, while background regions are areas of the images where the emissions are dominated by background emissions. Region size and shape are unique for each image as each ob-

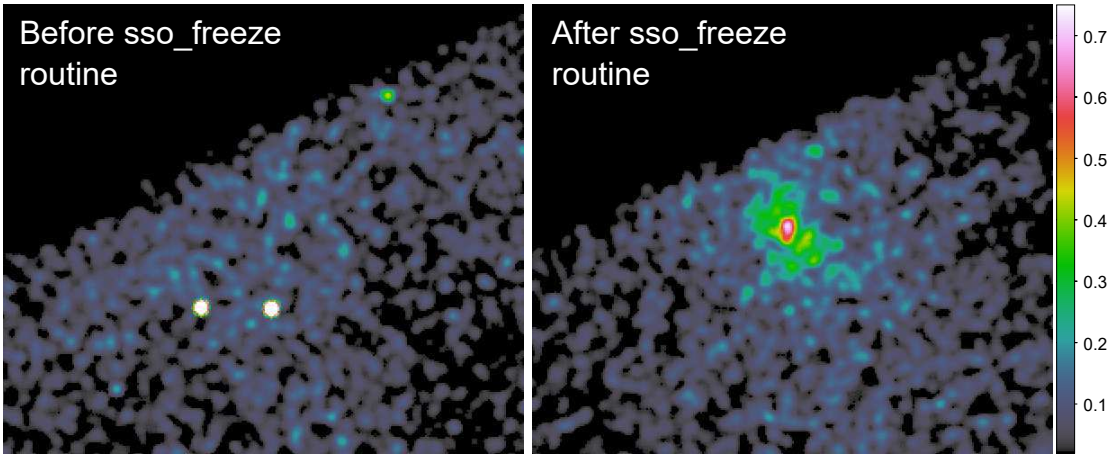

Fig. 2.1: An example of an image before and after running the *sso_freeze* routine from the CIAO software package. The process converts the image into the source object's rest frame, allowing for an accurate morphological spectroscopic analysis.

ject possesses unique morphology, chip positioning, and background conditions which make automation of region selection improbable. Instead, manual selection of both the source and background regions must be performed for each image. Designating between these two areas can be challenging for diffuse emission sources, such as comets, and so selected background regions should always be as far away from the source region as possible. However, it is assumed that a small percentage of source emission will still reside in the background regions, and this fact must be considered in future uncertainty calculations. In addition, background X-ray objects, such as stars, must be excluded from the regions through image masking to avoid contamination of our results. See Fig. 2.2 for an example of proper region selection, noting the streak down the

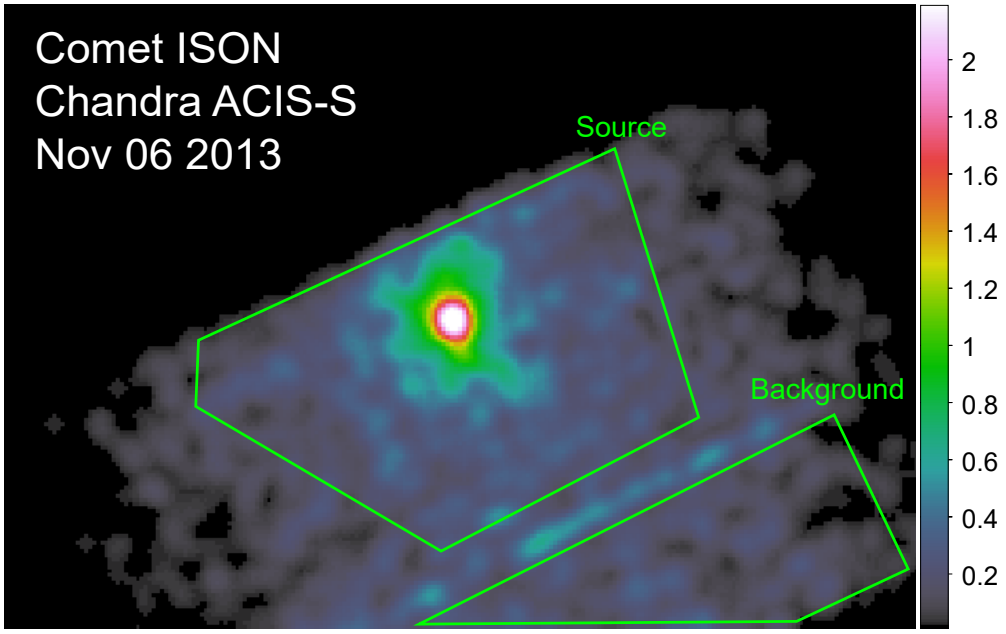

Fig. 2.2: An example of source and background region selection for image analysis. The source region is selected to encapsulate the emissions from the object of interest (in this case, comet ISON) while the background region is primarily free of source emissions. The streak in the image between the two regions is due to a background star moving in the comet's rest frame, which stresses the need for uniquely selected regions for each observation.

image center. This streak is due to a background X-ray object that appears as a diffuse streak after the image is reprocessed into the source object's rest frame. Exclusion of examples such as this are crucial for accurate morphological and spectral analysis, and the inconsistent nature of them in each image further reinforces the need for manual region selection.

2.4 Background Correction

When analyzing emissions from extended objects, such as comets or planetary atmospheres, one of two possible background correction techniques are frequently employed: on-chip corrections or blank-sky corrections. It is important to assess the benefits of each and determine which is preferred for our analysis.

On-chip correction is the most frequently utilized technique in X-ray emission analysis and is performed by isolating a region of pure background on the same chip that observed the source. A background spectrum, assumed to be constant over the entire area of the chip, is extracted from this region and subtracted from the raw source spectrum to create the final source spectrum. Such a method is valuable for X-ray analysis due to the high variability of X-ray background over time as it ensures near-identical background to that found in the raw source spectrum. However, observations of extended sources leave little area on chip for a proper background region to be defined. In the case of comet observations, the source may occupy 70–90% of the S3 chip, which reduces the possible background statistics one can gather and can increase the uncertainty in the resulting source spectrum. On-chip correction also requires scaling the calculated background count rates with the background-to-source region ratio. The background region ideally should be of similar or larger size to the source to avoid introduction of systematic error through this technique.

The alternative method is blank-sky background correction, which is performed by matching the coordinates of our comet observation to a similar blank-sky image

where only background emissions were observed. By scaling the blank-sky observation to the exposure map of our original observation, one can generate a synthetic background spectrum that can be utilized with our data. This technique is beneficial due to the low statistical uncertainty it introduces to our resulting spectrum. In addition, blank-sky correction is often preferred for extended sources, such as comets, as on-chip background regions may be contaminated by the source. Despite these benefits, the high variability of the X-ray background may result in blank-sky correction introducing random uncertainty into our calculations that would not exist from the on-chip method.

Analysis of both techniques shows that the spectral uncertainty introduced via on-chip correction only becomes significant at energies greater than 2 keV for high-intensity objects and 1 keV for low-intensity objects [3]. Since the emissions mechanisms discussed in this work primarily contribute in the 0.1-1.5 keV range, the on-chip correction method is preferred to avoid introducing additional uncertainty due to the X-ray background variability.

2.5 Emission Spectra Extraction

Having converted all images to object rest coordinates, corrected for exposure differences, and removed background counts, emission spectra may now be extracted. All spectra observations are taken by the *Chandra*-ACIS instrument, which has an approximate spectral resolution of 50 eV over the 0.3–2.0 keV energy range. Although this res-

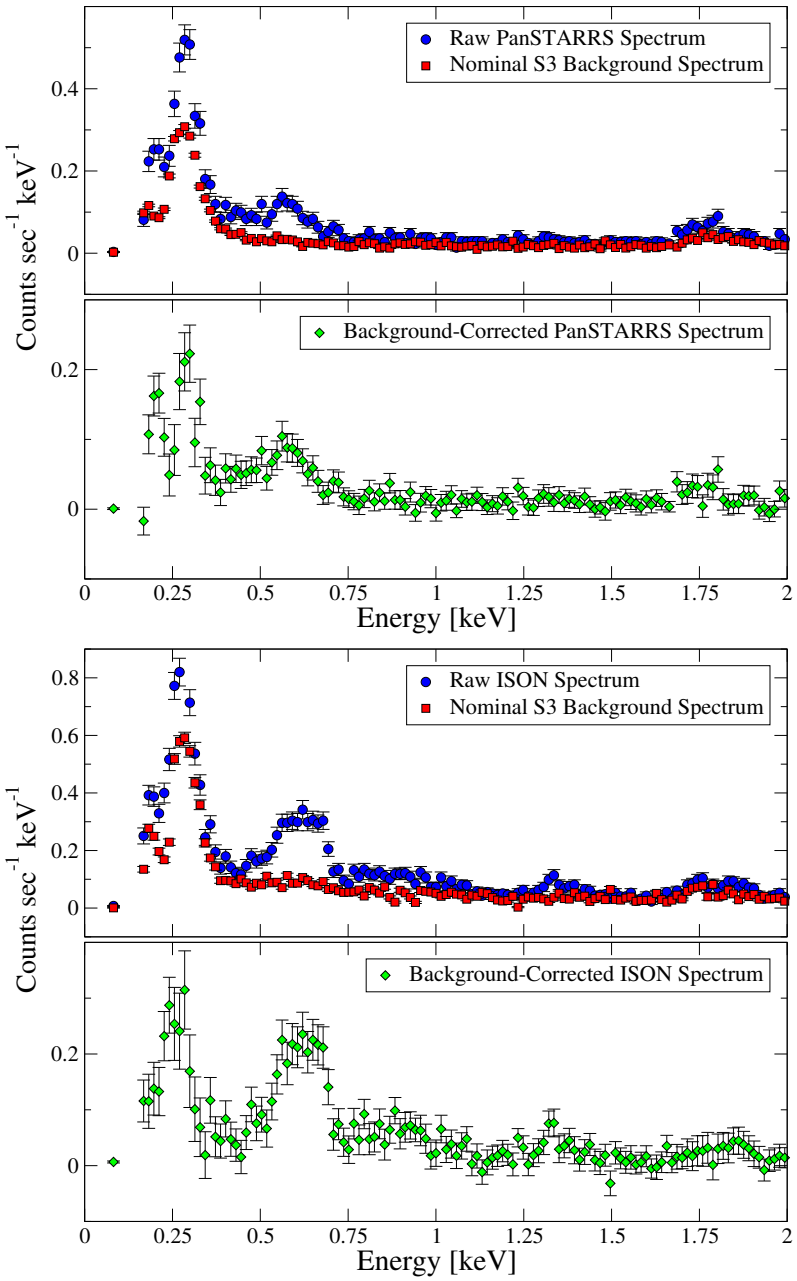

Fig. 2.3: Summed total spectra of X-ray photon counts for comets PanSTARRS and ISON extracted from *Chandra* observations. Both spectra utilize nominal S3 chip background emissions for background correction calculations.

olution is poorer than other X-ray observatories, *Chandra* provides improved count sensitivity that significantly improves signal-to-noise ratios, allowing for improved statistics when model fitting.

The emission spectra are generated by plotting the number of counts·sec^{-1} detected per energy bin over the desired energy range. These spectra can be obtained through summation of the raw counts per energy bin or through use of CIAO's *specextract* routine, which automates this process. Of the two processes, the latter is chosen. Spectra produced from multiple observations of the same object are combined with the *combine_spectra* routine to improve overall signal-to-noise ratios of the results. Examples of generated spectra from two comets are found in Fig. 2.3.

After obtaining the emission spectra, it is useful to convert the data into physical units for accurate comparison between other instruments as well as allow for proper physical modeling analysis. Conversion from counts to photons·cm^{-2} requires knowledge on the area of the telescope's field of view, but rarely is a telescope's geometric area considered accurate. Internal reflectivity and vignetting normally causes the geometric area of a telescope to be reduced to a smaller "effective area". Furthermore, effective area varies as a function of incident photon energy as the detector's quantum efficiency is not constant at all energies. Our resulting count rates per energy bin must be divided with the appropriate effective area for that energy when converting to physical units.

See Fig. 2.4 for a plots of the effective area functions for *Chandra*'s ACIS and

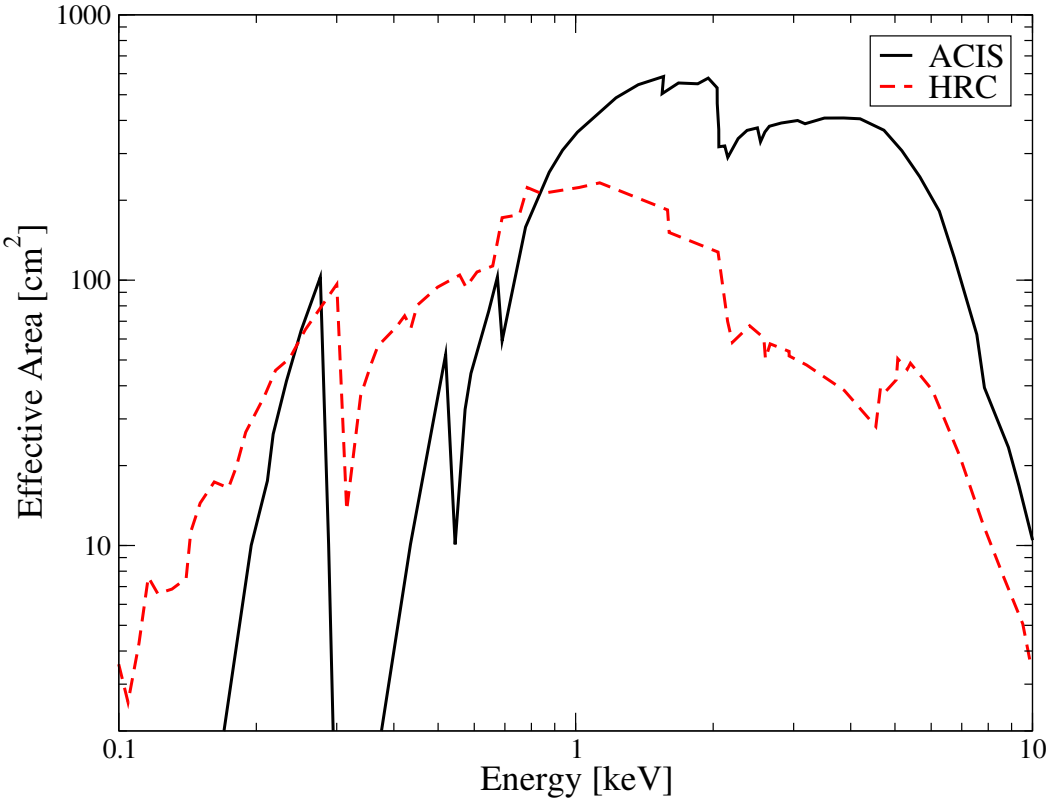

Fig. 2.4: A comparison of effective area functions for the ACIS and HRC instruments, as documented in the *Chandra* handbook. Note that HRC has a higher sensitivity to soft X-ray emissions than ACIS.

HRC instruments as of Proposal Cycle 18. As previously discussed in Sect. 2.1.1, the effective area function is dependent on the detector's efficiency, and this efficiency is known to degrade over time. As our analysis includes observations taken over the lifetime of *Chandra*, we therefore must utilize the effective area function that correctly corresponds to each observation. Previous effective area functions are available in the *Chandra* handbook and in CIAO. In addition, we note the significant difference between

the two plotted functions due to differing detectors and filters used. It is therefore important to always account for effective area when comparing results from different instruments, even if those instruments are on the same telescope. This fact will be important later in Sect. 5.8.

Chapter 3

Analysis of Charge-Exchange Mechanism

Charge-exchange (CX) is a common X-ray emission mechanism from local astronomical objects and a primary contributor to X-ray emission spectra, in some cases generating over 90% of the total intensity emission [4, 5, 6, 7, 8, 9]. Although common, these emissions have been shown to demonstrate high variability in intensity depending on local conditions near the source object [8, 10]. Therefore, accurate modeling of observed X-ray emission spectra must begin with a thorough analysis of CX and its dependence on various physical parameters.

3.1 Background

Nearly all local astrophysical objects generate an outward flux of particles through sublimation due to incident solar photons or solar wind (SW) particles on the object's surface. For planets, the majority of the outward flux will remain gravitationally bound while only highly energetic particles escape, creating a diffuse outflow above the high density atmosphere. For smaller objects like comets, the ejecta of atoms, dust, and ice

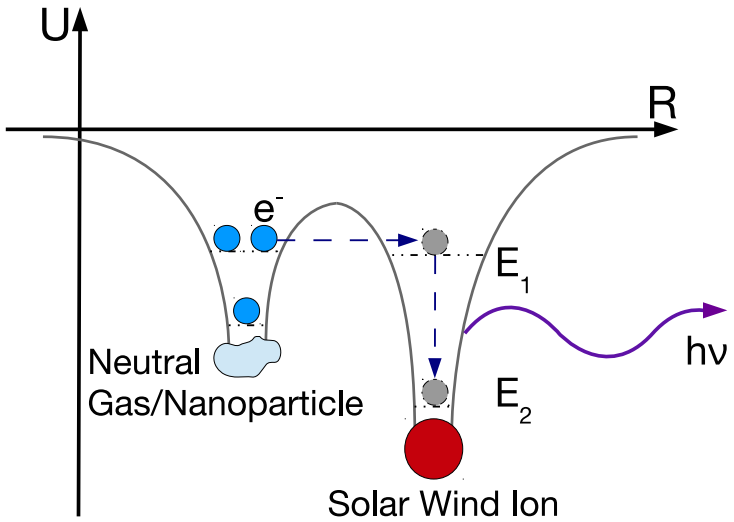

Fig. 3.1: A diagram of the Solar Wind Charge-Exchange (SWCX) process, in which an electron is transferred from a neutral particle to a solar wind ion. As the captured electron relaxes to its ground state, it will produce a high-energy photon that may be in the X-ray energy regime.

particles are not gravitationally bound and can create diffuse outflow of neutral material with velocities of a few km/s, often forming jet-streams from the surface [11].

As the flux of particles escape from their source object, they will begin to interact with an increasing density of SW ions. Should a neutral particle A quantum mechanically interact with a SW ion B^{N+}, it is possible for the neutral atom to exchange an electron with the ion, known as solar wind charge-exchange (SWCX) [5, 6, 7]. The process is illustrated with the equation

$$A + B^{N+} \rightarrow A^{+} + B^{(N-1)+^{*}}, \tag{3.1}$$

where the captured electron is in an excited state after the collision. Direct collision between the two particles may also produce a transfer of electrons, but it is much less likely of an occurrence. Either case will result in photons generated as the electron relaxes back to ground state. See Figure 3.1 for a diagram of this emission process.

Although SW is over 95% H^{+} and He^{2+} ions, there are highly charged and heavy ions, such as C^{6+}, N^{6+}, O^{7+}, O^{8+}, Mg^{9+}, and Ne^{9+}, present within the outward flux [12]. When these heavy ions undergo CX with neutrals, the relaxation energy is sufficient to generate X-ray emissions from the process. CX between these highly charged, heavy SW ions and neutral particles have been identified as the major source of emitted X-ray photons with energies below 1 keV [6].

3.2 Cross Sections

The CX process is dictated by the interaction cross section between the neutral particle A and the SW ion B^{N+}. The differential cross section is defined as

$$\frac{d\sigma}{d\Omega} = |f(|\vec{v_A} - \vec{v_B}|)|^2, \tag{3.2}$$

where $|\vec{v_A} - \vec{v_B}|$ is the relative speed difference between the particles.

Analytical solutions for CX cross sections are possible for simple, hydrogenic-like particles using the Landau-Zener formula to solve the transition dynamics of a

two-level quantum mechanical system. Higher order collisions can be approximated using Multi-Channel Landau-Zener Model, though the calculations quickly become difficult due to the increase in complexity of the electronic colliding structure and the complexity of the collision dynamics. As the focus of our work is on the application of these cross sections, we therefore use independently-calculated cross sections for various sources and targets for our modeling analysis [6, 13, 14, 15, 16, 17, 18, 19].

3.3 Spectral Intensity

The model of CX X-ray emissions discussed in this work is based upon previous modeling techniques [8, 20, 21, 22]. Though these previous models are robust, most only incorporate the primary emission lines, generally 10–20 lines, out of the possible 700+ lines that may be generated in an average CX interaction [6]. This is typically done because each emission line is treated as a free modeling fit parameter, and increasing the total number of parameters will significantly reduce confidence in any results due to chi-square testing. However, proper consideration of state selective CX cross sections of highly charged SW ions will reduce model fit parameters as all emission lines per ion will be set at fix ratios determined by their cross sections and photon emission yields [8]. Such a model would therefore only be dependent on the heavy SW ion composition, reducing the model from 700+ parameters down to 10-20.

The updated CX model developed through this work is generated from first principles that include all possible lines arising in radiative cascading processes of excited

SW ions with proper cross sections. This simplifies input parameters of X-ray modeling through limiting of input variables to SW ion composition while also improving its physical accuracy through the increase of emission lines. The model may also be utilized as a remote diagnostic tool for solar wind composition.

We begin by expanding upon the CX model outlined in previous works [8, 20, 21, 22]. The emitted intensity I of the photon flux induced by CX collisions is defined as the total emission resulting from the interaction between k species of atoms/molecules and SW ions l, where l is dependent on both the element and its charge. We define it as an integral over the line of sight distance s and the solid viewing angle Ω_s,

$$I(\hbar\omega_j) = \sum_{k,l} \int n_k n_l \sigma_{k,l} |\vec{v_k} - \vec{v_l}| P_{k,l}^{(j)}(\hbar\omega_j) ds d\Omega_s, \tag{3.3}$$

where n_k is the object of interest's particle density, n_l is the SW ion density at the object, $\sigma_{k,l}$ is the charge transfer cross section for collisions between k neutrals and l ions, v_k is the neutral particle velocity, v_l is the local SW velocity, and $P_{k,l}^{(j)}$ is the photon yield for emissions with the energy $\hbar\omega_j$ in the collision between k and l species. The total yield of all X-ray photons is normalized to unity, where $\sum_j P_{k,l}^{(j)}(\hbar\omega_j) = 1$, per each unique k and l in order to be valid on a per collisional basis.

For our equation, v_k is much lower than v_l and is therefore approximated as zero. The physical parameters $P_{k,l}^{(j)}$ and $\sigma_{k,l}$ are obtained from previous lab and theoretical research [6, 13, 14, 15, 16, 17, 18, 23, 24, 25, 26]. Calculation of n_l and v_l is highly dependent on the SW conditions at the time of observation, of which a discussion is

found in Sect. 3.4. The last term we require is n_k, and it is dependent on the source object. A discussion of neutral particle density distributions for diffuse atmospheres is found in Sect. 4.5. Applying these results, we are able to obtain theoretical or experimental values for each parameter in Eq. 3.3. We may therefore calculate the emitted intensity spectra for a local source object.

3.4 Solar Wind Conditions & Spectral Variability

The CX emission spectrum in our model is computed for two independent major groups of heavy SW ions:

1. (Group A): key heavy ions for "3/4 keV" energy interval (C^{5+}, C^{6+}, N^{5+}, N^{6+}, N^{7+}, O^{6+}, O^{7+}, O^{8+}, Ne^{8+},and Ne^{9+}). This group includes the CX emission spectra generated from collisions between neutrals and H-like, He-like, and Li-like heavy SW ions. The CX spectra of these ions are reasonably constrained by lab and theoretical research [6, 13, 14, 15, 16, 17, 18, 19].

2. (Group B): heavier excited ions (Mg^{q+}, S^{q+}, Si^{q+}, and Fe^{q+}) that primarily contribute to the soft X-ray spectra (below 0.4 keV). The cross sections and relative intensity of different emission lines of the CX cascading spectra for these ions are less known than for the ions from Group A but are well estimated [27, 28]. The energy position of spectral lines are well defined [29].

   The spectra of CX cascading photons for Groups A and B are computed inde-

Ion	Avg. Ratio[12]	Ion	Avg. Ratio[12]	Ion	Avg. Ratio[12]	Ion	Avg. Ratio[12]
C^{6+}	0.318	O^{8+}	0.070	Mg^{10+}	0.098	S^{9+}	0.019
C^{5+}	0.210	O^{7+}	0.200	Mg^{9+}	0.052	Fe^{13+}	0.002
N^{7+}	0.006	O^{6+}	0.730	Si^{10+}	0.021	Fe^{12+}	0.007
N^{6+}	0.058	Ne^{9+}	0.004	S^{11+}	0.005	Fe^{11+}	0.023
N^{5+}	0.065	Ne^{8+}	0.084	S^{10+}	0.016	Fe^{10+}	0.031

Table 3.1: Average slow solar wind ratios. All ratios are normalized with respect to the total solar wind oxygen composition.

pendently and then unified into a synthetic spectrum that represents the most probable emissions up to 1 keV. Ion elemental and charge composition for all groups are treated as variable parameters that are initially set to average SW composition ratios [12, 30]. The initial SW ratios for the model are shown in Table 3.1.

To calculate the CX emission intensity, accurate values for SW density and speed are also required. However, SW conditions are known to to have high variance as a function of both time and solar longitude. Therefore, only a direct observation of SW composition at the object of interest would be able to accurately determine the conditions present during the *Chandra* observations. As we lack such instrumentation, we approximate the SW conditions through use of the *Advanced Composition Explorer*, or *ACE*. *ACE* is a satellite located at the L1 Lagrangian point that continuously records SW conditions and stores all previous information in an online data archive. Although

ACE is not located at the object of interest, we evolve its data through use of time-of-flight correction models to approximate the SW conditions at the object [3]. We compare our results to average SW values taken from previous analyses of the SW plasma to ensure our results are physical [12].

After developing a physical range for these SW parameters, we allow the values to vary within these limits until a proper fit to the observational data is found over the 0.3–1.0 keV energy range. We define our goodness-of-fit with the χ^2 value, which is represented as

$$\chi^2 = \sum_{i=1}^{N} \left(\frac{x_i - \mu_i}{\sigma_i} \right)^2. \tag{3.4}$$

In this equation, the $x_i \pm \sigma_i$ is the observed data and μ_i is the modeled data. A low χ^2 value represents high confidence in the goodness-of-fit, and so we vary our parameters until χ^2 is minimized [3]. We note that due to Chandra's low sensitivity below 0.35 keV and the lack of accurate calibration near the carbon K-shell line at 0.284 keV, we find that varying several SW ions types that predominantly emit in this region produces no change in χ^2. As a result, these SW ion types are left constant as average SW composition ratios.

Chapter 4

Analysis of Scattering and Fluorescence Mechanisms

Coherent scattering and fluorescence (SF) of solar X-rays also contribute to the total observed X-ray emission spectra from local astrophysical systems, but their contributions at photon energies below 1 keV are minor when compared to CX [5, 31]. However, recent comet observations using *Chandra* have shown emission spectra above 1 keV with unresolved spectral features, or peaks [10]. Current interpretation of observed spectra suggest that these hard X-ray peaks are a result of CX with abnormal, highly ionized SW ions like Mg^{11+} and Si^{13+} [8, 10]. However, *in situ* observations with mass spectrometers have not detected these highly charged ions [30, 32]. Theoretical models describing the charge abundance of heavy SW ions also predict an extremely low probability of finding Mg^{11+} and Si^{13+} in the SW plasma because of the inability to reach such high freezing-in temperatures in regular SW and coronal mass ejections [12].

Alternatively, solar X-ray emissions with photon energies above 1 keV have been observed to increase by 1–3 orders of magnitude during solar flares [33]. It is therefore possible that SF emissions by heavy elements from an astrophysical environment would also increase by 1–3 orders of magnitude during high solar activity. Such an increase

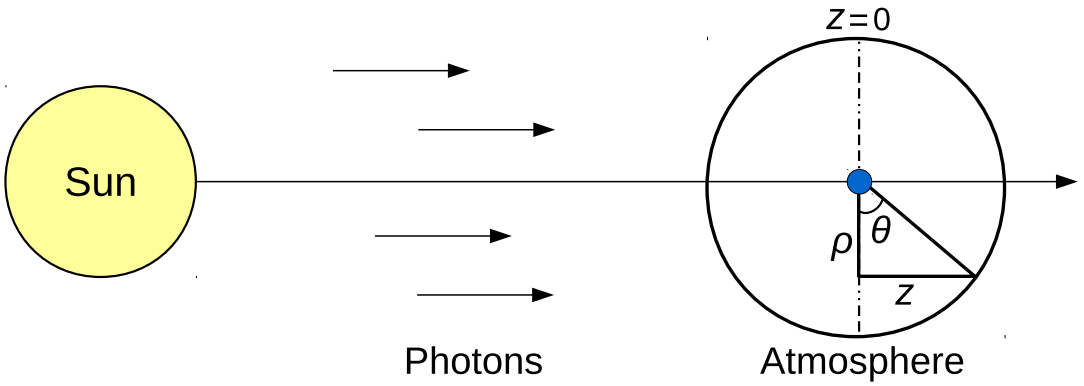

Fig. 4.1: Geometry of optical thickness calculations for a diffuse atmosphere. The variables listed are as follows: ρ is impact parameter from atmosphere center and z is the is half of the total penetration depth.

may result in SF providing more significant contributions toward X-ray emissions than CX. Accurate SF spectra of cometary X-ray emission should therefore be factored into spectral models.

This chapter will define the required parameters and characteristics of the solar X-ray emission spectra required for detailed formulation of the SF model and outline the model derivation.

4.1 Optical Thickness Approximation

We begin with an analysis of the optical depth of diffuse atmospheres, the primary sources of SF X-ray emissions. Assuming these systems are optically thin we may ignore radiative transfer processes in our emission model derivation, significantly simplifying our work.

We begin by defining optical depth τ as

$$\tau(z,\rho) = \int_{-\infty}^{z} n(z,\rho)\sigma_o dz, \tag{4.1}$$

where ρ is the impact parameter between the photon and the atmosphere center, z is half of the total penetration depth, and σ_o is the average cross section. A diagram of the physical setup is shown in Fig. 4.1. In principle, an optically thin atmosphere is defined as

$$\tau(z,\rho) << 1, \tag{4.2}$$

and so we will calculate τ and compare to this relation to determine the depth state.

We approximate the atmosphere as isotropic with a r^{-2} dependence, where r is defined by $r^2 = \rho^2 + z^2$. For this spherical atmosphere, we define the maximum radius as the mean ionization length of the neutral particles λ_{ioniz} as the ionized particles are carried away from the system via SW flows or the solar magnetic field. Utilizing our approximation, we define the average optical depth as

$$\langle\tau\rangle = \frac{1}{\pi\lambda_{ioniz}^2}\int_0^{\lambda_{ioniz}} 2\pi\rho d\rho \cdot \tau(z,\rho). \tag{4.3}$$

Combining Eqs. 4.1 and 4.3, we find

$$\langle\tau\rangle = \frac{\sigma_o}{\pi\lambda_{ioniz}^2}\int_0^{\lambda_{ioniz}}\int_{-\infty}^{z} 2\pi\rho n(z,\rho) dz d\rho, \tag{4.4}$$

which can further be simplified as the integration of scatterers over the entire atmosphere, which equals the total number of scatterers in the system N_{total}. This value may also be expressed as

$$N_{total} = \frac{Q\lambda_{ioniz}}{v}, \tag{4.5}$$

where Q is the neutral particle production rate and v is the neutral particle outflow velocity. Inputting our expression for N_{total} into Eq. 4.4 produces

$$\langle\tau\rangle = \frac{\sigma_o Q}{\pi\lambda_{ioniz} v}, \tag{4.6}$$

which is our general expression for optical depth.

Inputting a range of average values for diffuse atmospheres of both planetary and cometary origins, we find that $\tau \approx 10^{-(5-7)}$. This range of values is sufficient to satisfy Eq. 4.2, and so we may therefore assume that the systems we are to investigate in this work are optically thin. The description of thin atmospheres does not require consideration of the radiative transfer processes and allows us to calculate SF X-ray fluxes as a superposition of X-ray fluxes induced by independent single scatterers.

4.2 Cross Sections

Scattering properties for a particle are defined by its differential cross section

$$\frac{d\sigma}{d\Omega} = |f(\theta_{sc}, \epsilon)|^2, \tag{4.7}$$

which is dependent on scattering angle θ_{sc}, incident photon energy ϵ, and, for dust and ice particles, grain radius a. We assume that all dust and ice particles have spherical shapes as this approximation significantly simplifies the theoretical description of X-ray scattering. The scattering cross sections also depend on the polarization of incoming electromagnetic radiation. We consider the solar X-ray emission to be unpolarized and use, in our modeling, cross sections averaged over all polarization of solar X-rays. Differential cross sections of the atomic and molecular K-shell absorption, which determine fluorescence production rates, are isotropic and hence have no angular dependence.

Cross sections of elastic photon scattering and fluorescence for all atoms and some molecules have been measured in laboratory experiments and/or been calculated using accurate quantum mechanical methods and many-body theory. For atomic constituents, we utilize well-established databases [34, 35]. These databases are known to lack accuracy with energies close to resonance transitions, but averaging of accurate near-resonance structures over energy step sizes comparable to our selected databases provide good agreement [36].

Data on scattering of X-rays by dust and ice particles is significantly less developed and is mostly based on empirical models [37, 38]. The classical Mie model is used as an approximation in determining differential and total cross sections for nano-sized dust and ice particles [39], although differences between the results of Mie and quantum calculations are expected for ultra-small grains. While real nanodust and ice

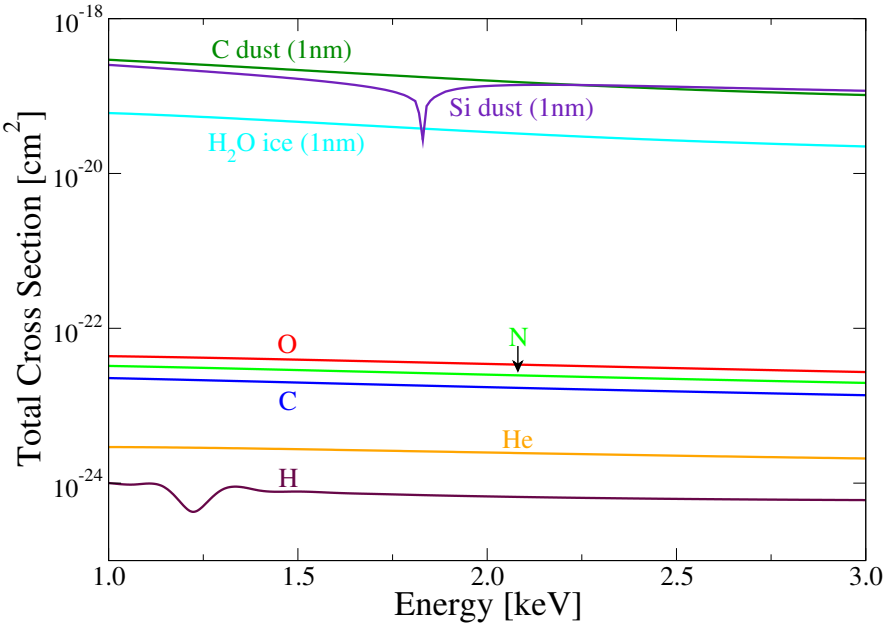

Fig. 4.2: Total cross sections for X-ray scattering of both nano ice and dust as well as neutral hydrogen, helium, carbon, nitrogen, and oxygen gases.

may have extremely complex compositions and geometries, ranging from relatively simple core-mantle structures to large aggregates [40], we choose to model the particles as Mie spheres. Such a Mie model assumes a spherical, homogeneous scatterer with uniform index of refraction and is the exact solution to Maxwell's equations [41]. Realistic nanoparticles are not spherical and may form much more complex structures, thus requiring a more rigorous calculation of classical scattering methods [39, 42], but use of homogenous dust/ice spheres and the Mie model allows for a good approximation of scattering cross sections. The Mie spheres range in radii from 1–10 nm and are composed of carbon, silicon, and H_2O ice. The index of refraction used for the nanodust spheres is obtained assuming bulk densities and is dependent on incident photon

energy [43]. Detailed information on scattering cross sections of nanoparticles and relevant atmospheric gases is provided in Fig. 4.2.

4.3 Spectral Intensity

In our model, the object of interest center is located at a distance r_c from the Sun and the detector-Sun distance is R_0. See Fig. 4.3 for a diagram of the scattering geometry. The scattered spectral intensity is defined as the number of photons collected per second per unit surface area and per unit interval of the photon energy ϵ. If the solar spectral intensity is known at some specific distance from the Sun, for example at $R_0 = 1$ AU, we can define the observed scattered intensity radiation as seen at the detector $I_{sc}(\epsilon)$ in terms of the known solar spectral intensity $I_0(\epsilon)$. The value of $I_{sc}(\epsilon)$ is given by the sum of all photons scattered by atoms, dust, and ice particles.

The spectral intensity $I_{sc}(\epsilon)$ of X-rays scattered by the diffuse atmosphere is found by integrating over the entire atmospheric volume with the density distribution $n_j(r)$ for j types of scatterers:

$$I_{sc}(\epsilon) = I_0(\epsilon) \sum_j \int n_j(r'_j) \frac{R_0^2}{|\vec{r'_j} + \vec{r_c}|^2 |\vec{r'_j} + \vec{r_c} - \vec{R_0}|^2} |f_j(\theta'_{sc}, \epsilon)|^2 d^3 r'_j. \tag{4.8}$$

Equation 4.8 is valid for optically thin atmospheres, where scattering and absorption of X-rays do not affect the value of the local X-ray photon flux.

Simplification of Eq. 4.8 occurs if the atmosphere's size is small with respect to distances r_c and $|\vec{r_c} - \vec{R_0}|$: $r_j << r_c, |\vec{r_c} - \vec{R_0}|$. This assumption is, in principle, valid

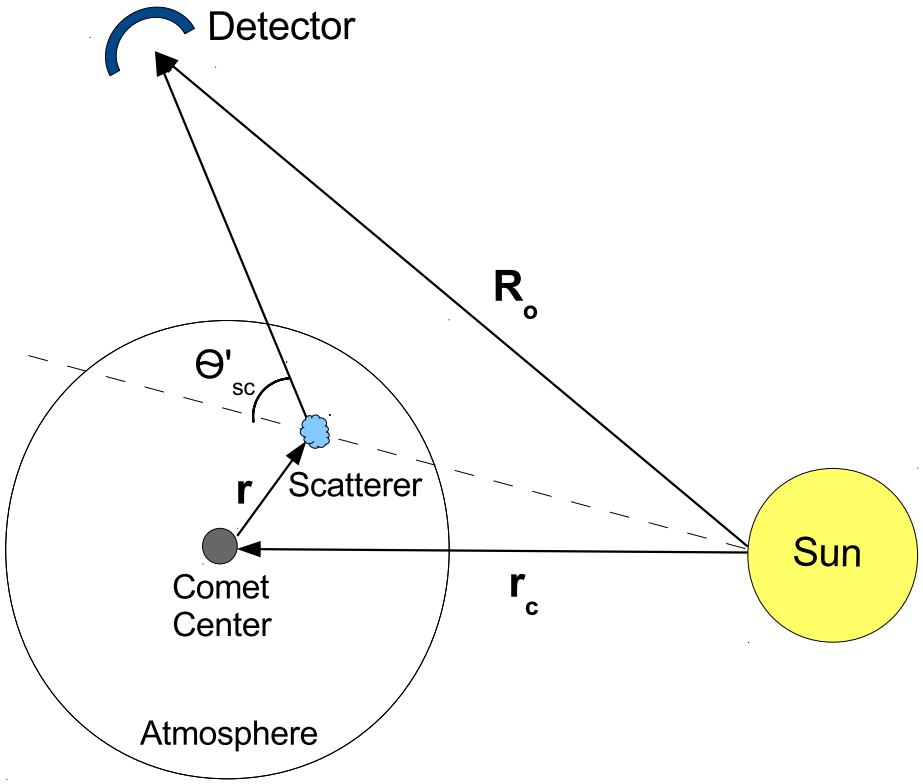

Fig. 4.3: Geometry of a single scatterer within an atmosphere (in this case, a cometary atmosphere). The variables listed are as follows: $\vec{R}_0$ is the Sun-detector distance, $\vec{r}_c$ is the Sun-object center distance, $\vec{r}$ is the object center-scatterer distance, and Θ'_{sc} is the scattering angle.

in regards to diffuse emissions from any local astrophysical objects. For comets, the radius of the atmosphere r is $\sim 10^{5-6}$ km when the object is $\sim$1 AU from the Sun. In comparison to the distances r_c and $|\vec{r_c} - \vec{R_0}|$ that we used in our analysis, the cometary atmosphere is 2–3 orders of magnitude smaller in size. For planetary emissions, the ratio is even smaller, often 5–6 orders of magnitude. As our SF analysis is focused on emission spectra and not the numerical modeling of emission morphology of emissions, we may approximate the atmosphere as a point source located at r_c and comprised of N_j number of scatterers. Applying this approximation to Eq. 4.8, we obtain a simple expression for the spectral intensity of scattered X-ray photons:

$$I_{sc}(\epsilon) = I_0(\epsilon)\frac{R_0^2}{r_c^2|\vec{r_c} - \vec{R_0}|^2}\sum_j |f_j(\theta_{sc}, \epsilon)|^2 N_j. \tag{4.9}$$

The resulting equation is an approximation of the scattered X-ray intensity and is a valid approximation in all the cases that we will investigate.

The derivation of fluorescence emissions is identical to that of scattering, except we are now interested in the intensity I_{mk} of a specific spectral line rather than the spectral intensity. The total intensity per fluorescence line k of scatterer m is defined as

$$\mathit{I}_{mk} = \frac{R_0^2}{r_c^2|\vec{r_c} - \vec{R_0}|^2} N_m \int_{\epsilon_k}^{\infty} |f_m(\epsilon)|^2 g_{m,k}(\epsilon) I_0(\epsilon) d\epsilon, \tag{4.10}$$

where the intensity spectrum is integrated from the threshold energy ϵ_k of absorption for the considered fluorescent photon ϵ_{0_k}, to infinity. As the solar intensity spectrum and photo-absorption cross sections drop off significantly at large ϵ, we truncate the upper

bound at 10 keV. The fluorescence intensity is also dependent on the fluorescence yield $g_{m,k}(\epsilon)$, the efficiency of many-electron Auger transitions [44]. Fluorescence yield determines the probability of photon emission by excited many-electron ions. Equations 4.9 and 4.10 allow calculation of a complete SF emission spectrum from a diffuse atmosphere.

4.4 Variability of Spectra due to Scatterer Composition

Every atmosphere has a unique mixture ratio of atoms, dust, and ice particles, which is a function of the object-Sun distance and object composition. As cometary atmospheres nearing perihelion with the Sun possess both favorable observation geometry and are optically thin sources, they are the most likely candidate for detection of significant scattering emissions [45]. We therefore focus our discussion on cometary composition. In principle, the same analysis would be valid for any diffuse emissions, albeit with the initial composition adjusted to match the object of interest.

On average, comets are shown to be primarily composed of H_2O, with an average atmospheric contribution of 85% [46, 47, 48]. Carbon amounts vary between the comets [46], averaging to be 10% of the total atmosphere. Nitrogen and silicon are also present in trace amounts, composing less than 5% of the atmosphere.

We normalize the H_2O production rate Q_{H_2O} to observed rates for each comet [46, 47, 48]. All other element production rates are set equal to the average element-to-H_2O composition ratio multiplied by Q_{H_2O}. We note that because of this normalization

method and the overwhelming percentage of H_2O in the cometary atmosphere, variations in the mixture ratio of minor elements produce only slight changes to our results. We also choose to exclusively model O-based fluorescence because of the significant proportion of O present within cometary atmospheres in relation to all other elements present.

While micron-sized cometary dust particle densities are well-studied due to their efficient scattering of infrared and optical radiation, nano-sized dust and ice particle densities and composition ratios are not as well-established because of a lack of precise observational data for such small masses [49]. Nanoparticles also efficiently scatter X-rays because their grain geometric sizes are on the same scale as the photon wavelengths [31, 39] and are therefore the focus of our scattering calculations. For our model, we infer that dust particles would maintain a similar ratio to those observed for atoms, with 85% H_2O, 10% C, and 5% heavier elements like N and Si. Unlike dust particles that can be composed of a variety of elements, ice particles are mostly composed of H_2O or CO_2. Modeling of ice particles has shown dissociation rates to be dependent on their impurity ratios, where particles with a minimum impurity ratio, known as pure ice particles, possess the longest lifetime [50]. In our consideration of X-ray scattering by dust and ice nanoparticles, we initially treat all ice particles as pure to establish an upper limit on the particle densities. Should the total scattered contribution of these particles prove significant, we will revise our model to include more accurate impurity distributions.

As observational dust and ice mass production rates within cometary atmospheres are not well-studied, the mass production rate of dust particles q_{dust} is unknown for each of the five comets we analyzed. Instead, the empirically established proportionality for mass loss rates $q_{dust} \simeq 1.5 q_{gas}$ is used to estimate the total number of nanoparticles present within the atmosphere [5, 31, 51]. This relationship has previously been shown to be valid for micron-sized dust particles down to 0.1 μm [38] and is extrapolated down to nanoparticles for our analysis. The extrapolated total nanoparticle mass loss rate agrees with measurements from Utterback and Kissel [49], but it is possible that nanoparticle distributions may behave independently from micron-sized grains. We therefore use this empirical proportionality for our initial results and then will vary nanoparticle densities as a free parameter when comparing to *Chandra* data.

4.5 Scatterer Density Distributions

Spatial distribution of the scattering gas, molecules, and dust/ice particles depend on several factors, the most important one being the interaction of the local environment with solar radiation and SW. Accurate modeling of an atmosphere requires:

1. A detailed description of the formation of the gas and dust fluxes on the host object surface;

2. Analysis of important chemical and photo-chemical reactions, as well as dust and ice-particle fragmentation processes;

3. modeling of the SW plasma interaction with a dusty atmosphere, using advanced MHD models [52] or direct Monte Carlo simulations [53].

Our investigation of X-ray emissions is focused on determining spectral intensities, so the X-ray morphology and spatial distributions of the gas and dust can be considered approximately. As a result, we use a simplified model of the distributions, assuming the size of the diffuse atmospheres to be much smaller than r_c and $|\vec{r_c} - \vec{R_0}|$. The density distribution is modeled differently for gas and nanoparticles. The total atomic and molecular gas density $n(r)$, composed of j unique scatterers, is defined with a simple radial distribution [4],

$$n(r) = \sum_j n_j(r) = \sum_j \frac{Q_j}{4\pi v_j r^2} e^{-r/\lambda_{m_j}}, \tag{4.11}$$

where Q_j is the particle production rate for scatterer i, v_j is the radial flow velocity of the scatterer, r is the radius from the object center, and λ_{m_j} is the mean ionization length for the scatterer.

Distributions $n(r)$ for dust density and dust radius, a, are taken from Fink and Rubin [38],

$$n(r, a) \sim \frac{a^{-\alpha}}{r^{\beta}}, \tag{4.12}$$

where α is set to 2.5 and β is set to 2.0. This distribution agrees with interpolated results extracted from Rubin et al. [37], although normalization was required. The normalized density distribution $n_j(r, a)$ for j dust and ice scatterers is determined to be

$$n_j(r,a) = \frac{|\alpha - 1|}{4\pi a_l r_u^3} \left(\frac{a_l}{a}\right)^{\alpha} \left(\frac{r_u}{r}\right)^{\beta} N_{d_j}, \tag{4.13}$$

$$\int n_j(r,a)\, da\, d^3r = N_{d_j}, \tag{4.14}$$

where a_l is the lower bound for the particle grain radius and r_u is the upper bound for the atmosphere radius. Integrating over all grain radii and assuming a simplified model of strictly spherical dust particles, an atmospheric volume for scatterer j equals the total number of dust particle j in the atmosphere N_{d_j}. The total volume density-size distribution of dust and ice particles can be calculated by a summation of Eq. 4.13 over all types of nanoparticles present within the system: $n(r,a) = \sum_j n_j(r,a)$.

4.6 Solar X-Ray Intensity

Spectral composition and intensity of solar X-rays are important for calculating the total SF spectrum of X-ray emission. The CHIANTI atomic database, a theoretical emission line database specifically designed for astrophysical plasmas, is used to model the relative spectral intensities (spectral shape) of the X-ray spectrum from 0.3–2.0 keV [54, 55]. We compare the modeled spectrum to observational data from McKenzie et al. [56] taken from *SOLEX-A*, and both are in good agreement. Slight discrepancies present are likely a result of fluctuations of solar X-ray line intensities which naturally occur over time [33].

The results from McKenzie et al. [56] and CHIANTI provide a reliable database from which we can extrapolate a spectral shape, but the solar X-ray spectrum during

observations is highly dependent on the solar conditions at the time of detection. It is therefore important to determine the real-time solar X-ray intensities during observations and to scale the modeled SF spectra to these values. The *GOES X-Ray Satellite* records total X-ray intensities over the 1.5-15.0 keV range as seen at Earth in three-minute intervals and has data on solar conditions during each observation that we are analyzing. By correcting for time-of-flight differences between *GOES* and the object of interest and also normalizing our model's spectral intensity to match the observed intensity of *GOES*, we may approximate the solar spectral intensity emitted during each observation [45]. Similar to our results for CX, we again note that these approximations assume the object of interest encountered similar solar conditions to those observed near Earth. This assumption may not be the case due to the highly non-isotropic nature of solar emissions, but our approximation provides us with the best estimate for solar intensities at the object given the tools provided.

Chapter 5

Cometary Observations and Analysis

Cometary X-ray emissions, originally discovered by Lisse et al. [57] and now observed in over 30 comets, are a well-studied phenomenon. As comets pass through the solar system, they absorb solar energy and eject atoms, dust, and ice particles through sublimation. Fluxes of neutral material created at the nuclear surface propagate outward with velocities of a few km/s and can form localized jet-streams of ejecta from the comet's surface [11]. This neutral ejecta forms a diffuse cometary atmosphere that undergoes significant transformation because of photo-chemical reactions, dissociation of molecular species, and fragmentation of dust and ice particles.

The neutral gas that composes the cometary atmosphere has been shown to produce X-ray emissions from both CX and SF [4, 5, 6, 7, 8, 9]. CX emissions are generated from collisions between highly charged, heavy SW ions (~0.1% of all solar wind ions) and the neutral gas. CX has been shown to be the dominate emission mechanism over the 0.3–1.0 keV energy range, with CX producing over 95% of the total observed intensity [5, 6, 7]. SF of solar X-rays also contribute to the observed X-ray intensities, but their contributions at photon energies below 1 keV have been estimated to be a

minor fraction of the total flux of cometary X-rays [5, 31].

Although the analysis of CX emissions is well-established, new and valuable insight can be obtained from the data. Through the use of our developed model, we may obtain information regarding SW composition at the comet during observations, a feat that would normally require a local detector due to highly nonuniform solar emissions. This advanced probing of SW composition would be applicable to any astrophysical system which is emitting due to CX, allowing for probing of distant systems that are unrealistic to analyze with a local detector. Such mapping of SW conditions would be of significant use to the astronomical branch of stellar wind modeling, a challenging area of physics due to the lack of required simultaneous data points over a wide area. In addition to this massive benefit, our model provides reductions in computational time to fit observational data while improving the physical accuracy of our results. This makes our efforts valuable for multiple areas of research as more physical insight into our local universe can be extracted from already available databases of observations.

Beyond using CX as an analysis tool, SF emissions also present a unique opportunity to extract new physics for comets, as well as dust and ice particles. As previously discussed in Chapter 4, SF emissions may be detectable from comets at energies greater than 1 keV due to their diffuse atmospheres and close proximity to both the detector and Sun. This presents us with an unique opportunity to extract accurate SF emission spectra from astrophysical sources, which would provide accurate estimates on particle mass loss rates from the comet and particle density distributions. These results may

provide valuable insight on properties like densities, cross sections, and grain size dependence of the dust and ice particles present within these systems . Even though dust and ice are present in nearly all astrophysical systems, little is understood about them when approaching nano-sizes due to a lack of detector sensitivity from *in situ* observations [49]. Having a better understanding on production rates, lifetimes, and densities (all of which would be possible from these results) would go a long way to improving our knowledge on these elusive particles.

Given these substantial benefits from investigating comets with our newly developed models, it is no surprise we selected several unique and/or bright cometary observations that will allow us to test the validity our models and also comment on the validity of the possible benefits beyond cometary physics.

5.1 Modeled Average Emission Spectrum

Before analyzing emissions from various comets, we must first ensure our emission model produces physically consistent results. We therefore begin with Fig. 5.1, which is the output emission for an average comet encountering average solar conditions at a distance 1 AU from both the Sun and the detector. As the figure shows, our model below 1 keV has CX as the dominant emission mechanism by orders of magnitude. The resulting emissions are consistent with independently calculated values [5] and agree with our previous assessment that CX would be the primary mechanism. Curiously, scattering from nanoparticles appears to contribute significantly less than from

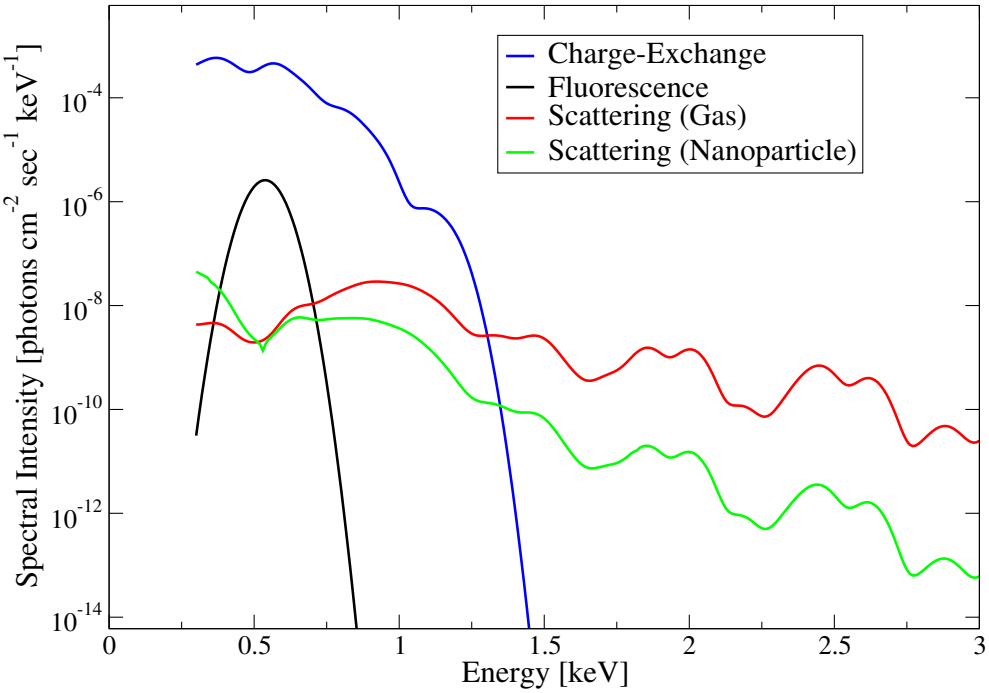

Fig. 5.1: A modeled cometary emission spectrum for an average cometary observation.

gas scattering. To confirm that this result is not a byproduct of of the non-isotropic nature of the dust and gas cross sections, this average emission spectra is generated at several different scattering angles. In each case, the nanoparticle emissions are found to be noticeably lower than those from the gas. We therefore conclude that the nanoparticle densities present in an average cometary system should be incapable of producing detectable emissions. An investigation of increased nanoparticle densities and inclusion of total dust emissions is explored in further detail in Sect. 5.3.

5.2 Modeled Average Emission Morphology

Beyond analysis through spectroscopic modeling, observational data should also be compared to approximate morphological models as cometary emission morphology strongly correlates to SW conditions during the observations [7, 9, 58]. A simplified theoretical description of interaction between the SW plasma and cometary atmosphere shows that the emission originates predominantly from the sunward hemisphere of the neutral coma and creates a projected paraboloid of emission with the comet at its focal point [52, 58].

To generate an approximate cometary emission morphology, we begin by dropping the exponential term from the cometary gas production rate defined in Eq. 4.11, producing

$$n_g(r) = \frac{Q}{4\pi v_g r^2}, \tag{5.1}$$

as we are only concerned with the local emissions from the comet nucleus. Since we recall CX emissions to be the dominant source of intensity, we then return to our CX intensity equation, Eq. 3.3, for our description of the morphology. We simplify this equation by assuming all CX interactions emit a photon of average energy E, producing

$$I = n_g n_{sw} \sigma_{avg} |\vec{v_{sw}} - \vec{v_g}| E, \tag{5.2}$$

where n_g is the cometary gas density, n_{sw} is the SW density, and σ_{avg} is the average CX

cross section for the system. We may further simplify this equation by realizing the SW velocity $\vec{v_{sw}}$ is normally 2 orders of magnitude greater than the gas outflow velocity $\vec{v_g}$, even during periods of slow SW speeds. We may therefore simplify Eq. 5.2 to

$$I = n_g n_{sw} \sigma_{avg} v_{sw} E. \tag{5.3}$$

and we now only require n_{sw} to model Eq. 5.3.

To solve for n_{sw} for this simplified system, we assume all SW ions are traveling in a parallel flow. The SW ion density then may be defined as the differential equation

$$\frac{dn_{sw}}{dt} = -n_g n_{sw} \sigma_{avg} v_{sw}. \tag{5.4}$$

We define the +x direction as the interacting line from the comet to the Sun, and so $v_{sw} = -dx/dt$. Substituting in both our equations for v_{sw} and n_g results in

$$\frac{1}{n_{sw}} \frac{dn_{sw}}{dx} = \frac{Q\sigma_{avg}}{4\pi v_g r^2}. \tag{5.5}$$

Solving this differential equation in comet-centered cylindrical coordinates produces the expression

$$n_{sw} = n_{sw,0} exp\left(-\frac{Q\sigma_{avg}\theta}{4\pi v_g r sin\theta}\right). \tag{5.6}$$

where $n_{sw,0}$ is the initial SW density prior to interacting with the cometary atmosphere. Combining Eqs. 5.1 and 5.6 with 5.3 gives us

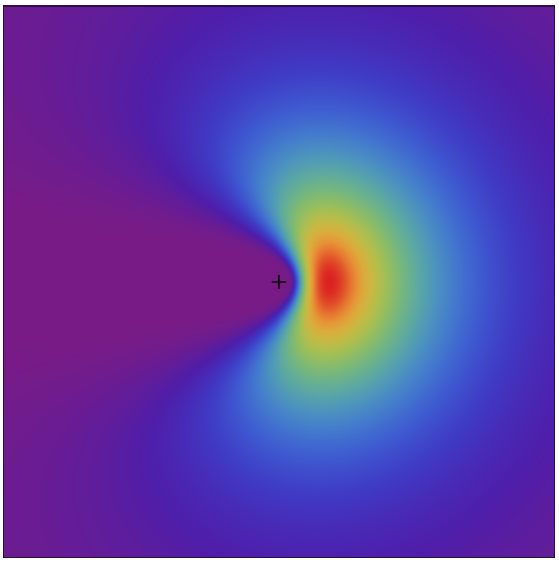

Fig. 5.2: A modeled cometary emission morphology for an observation of an average, collisionally thick cometary atmosphere. The comet is located at the center, while the Sun (not shown) is to the right.

$$I = \frac{Qn_{sw,0}\sigma_{avg}v_{sw}E}{4\pi v_g r^2} exp\left(-\frac{Q\sigma_{avg}\theta}{4\pi v_g r sin\theta}\right), \tag{5.7}$$

which we may use as an approximate model of cometary X-ray emissions. See Fig. 5.2 for an image of the modeled cometary emission.

When analyzing cometary X-ray images, the overall emission morphology is determined by SW interaction with the cometary atmosphere as the majority of the emitted intensity is due to CX. In the collisionally thick case for an active comet, we expect a paraboloid with the comet at the focus where the magnitude of the semimajor axis is dependent on the atmospheric density [47, 52, 58, 59]. We may therefore assume that any observations with a similar structure to our model possesses high interaction

rates between the SW and neutral atmosphere.

In comparison to our modeled case, the collisionally thin case will produce the majority of its X-ray emission structure at its highest concentrations of gas in the coma. For such a situation, we expect to see regions of enhanced X-ray emission at regions of higher cometary particle density, such as those found along jet streams near the cometary surface [60]. As neutral outflow morphology is dependent on shape, structure, and composition of the comet, each collisionally thin cometary atmosphere possesses an irregular emission morphology that cannot be easily quantified without more information on the system. Nonetheless, the lack of predictable emission morphology is still a strong indicator of below average SW and/or neutral particle densities present during the observation.

5.3 Ikeya-Zhang

Having developed models that accurately reproduce emissions from cometary systems, we now begin comparing our results to observational data. All comets selected have previously been observed via *Chandra* and are openly available for use on the *Chandra* Data Archive. Details regarding selected comets are outlined in Table 5.1. Of the comets we selected, the *Chandra* observations of comet Ikeya-Zhang (IZ) are of significant interest because of the high cometary X-ray intensity and pronounced spectral shape established from previous analysis [10]. Data on X-ray intensity emissions from *GOES* taken at the same time as the *Chandra* observations of IZ show that 2–4 M-class

Comet	Obs. Date	Prop. Num.	$T_{\rm exp}$ (ks)	$r_{\rm c}$ (AU)	Δ (AU)	$\rm Lat_\odot$ (deg)	$\rm Long_\odot$ (deg)	$Q_{\rm H_2O}$ (10^{28} mol $\rm s^{-1}$)
8P	2008 Jan 01–04	09100452	47	1.10	0.25	2.076	89.22	2.2[48]
Encke	2003 Nov 24	05100560	44	0.89	0.28	11.41	50.19	0.7[47]
ISON	2013 Oct 31–Nov 6	15100583	36	1.18	0.95	1.130	115.0	2[61]
IZ	2002 April 15–16	03108076	24	0.81	0.81	26.42	205.0	20[46]
LS4	2000 July 14	01100323	9.4	0.80	0.53	24.18	312.6	3[62]
MH	2001 Jan 8–15	02100340	16.9	1.26	1.37	13.50	185.1	12[46]
PanSTARRS	2013 Apr 17–23	14108442	45	1.10	1.44	84.16	150.5	5[63]

Table 5.1: Observation parameters are listed as follows: *Chandra* observation date, observation proposal number, exposure time $T_{\rm exp}$, comet-Sun distance $r_{\rm c}$, comet-Earth distance Δ, Heliospheric Latitude $\rm Lat_\odot$ and Longitude $\rm Long_\odot$, and H_2O production rate $Q_{\rm H_2O}$.

solar flares occurred during this time. The cometary X-ray scattering flux of M-type X-ray solar flares can be 1–3 orders of magnitude higher than the flux observed during quiet solar conditions. In addition, IZ had the highest observed particle production rates of any other comet analyzed [46], providing additional atmospheric scatterers. It therefore should possess an unusually high signal-to-noise ratio, producing improved modeling statistics as well as optimal conditions for the detection of SF emissions.

Morphology

The ACIS observation image of comet IZ is presented in Figure 5.3. The image has been corrected for differences in exposure time, smoothed with a 3×3 pixel Gaussian

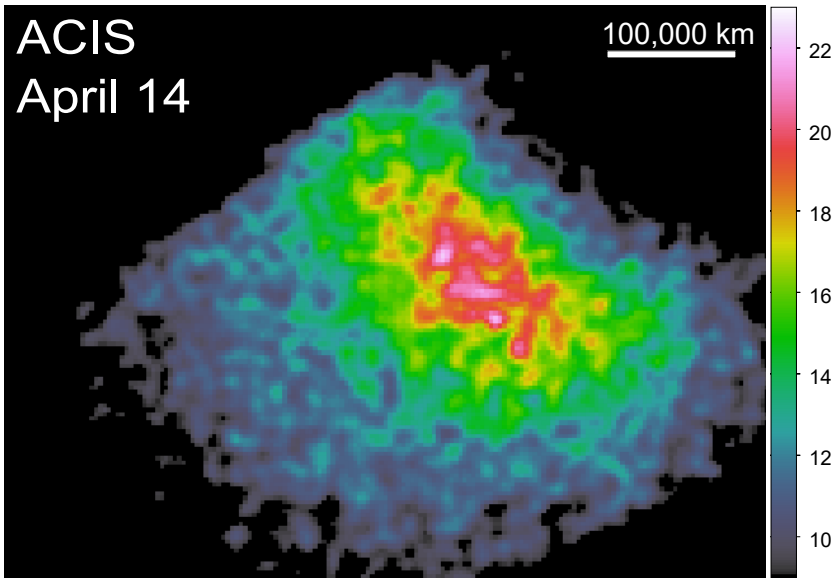

Fig. 5.3: *Chandra*/ACIS-S observations of comet Ikeya-Zhang. The images are binned to include all 0.3–2.0 keV photon events, exposure corrected, on the same linear scale, and smoothed with a 3×3 pixel Gaussian filter. Our results show an abnormally high X-ray emission intensity with the predicted paraboloid shape.

filter, and is shown on a linear scale. This image is highly abnormal for a cometary observation as the total intensity from IZ is 2–3 orders of magnitude larger than average. This increase agrees with our previous assessment that the increase in particle production rates from the comet coupled with the high solar activity at the time of observation should result in increased X-ray emissions.

In addition to the intensity, IZ's image serves as an excellent example of the ideal emission morphology from a collisionally thick cometary atmosphere. We clearly see the projected paraboloid shape, with the comet nucleus located at the center. This

structure extends farther out than is seen in other cometary observations, indicating above average SW density, above average particle density, or possibly both. Regardless, IZ is the benchmark case of cometary morphology to which all others are compared.

Emission Spectrum

As we have established, comet IZ demonstrated above emission activity during the course of its *Chandra* observations. With such a high signal-to-noise ratio, IZ's emission spectrum allows for unparalleled probing of cometary emission mechanisms contributions to high accuracy. We therefore analyze each emission mechanism individually in order to properly assess contributions from each one.

Analysis of Charge-Exchange Emissions

Utilizing our CX model, we are able to successfully describe the IZ emission spectrum, as shown in Fig. 5.4. We find a unique solution for the emission spectrum that fits well to the observations up to 1.0 keV. We also calculate the reduced χ^2, also known as χ^2_R, by dividing χ^2 with the degrees of freedom (dof) for each comet. The comet observations are binned with a minimum of six counts per spectral bin for proper gaussian statistics. For IZ, which has 32 dof, $\chi^2_R = 1.2$ for the 0.35–1.00 keV range. All spectra are truncated at 0.35 keV due to the carbon K-shell absorption edge detector contamination present from ACIS at energies below this threshold. These results agree well with previously calculated emission spectrum models for IZ [10] while also pro-

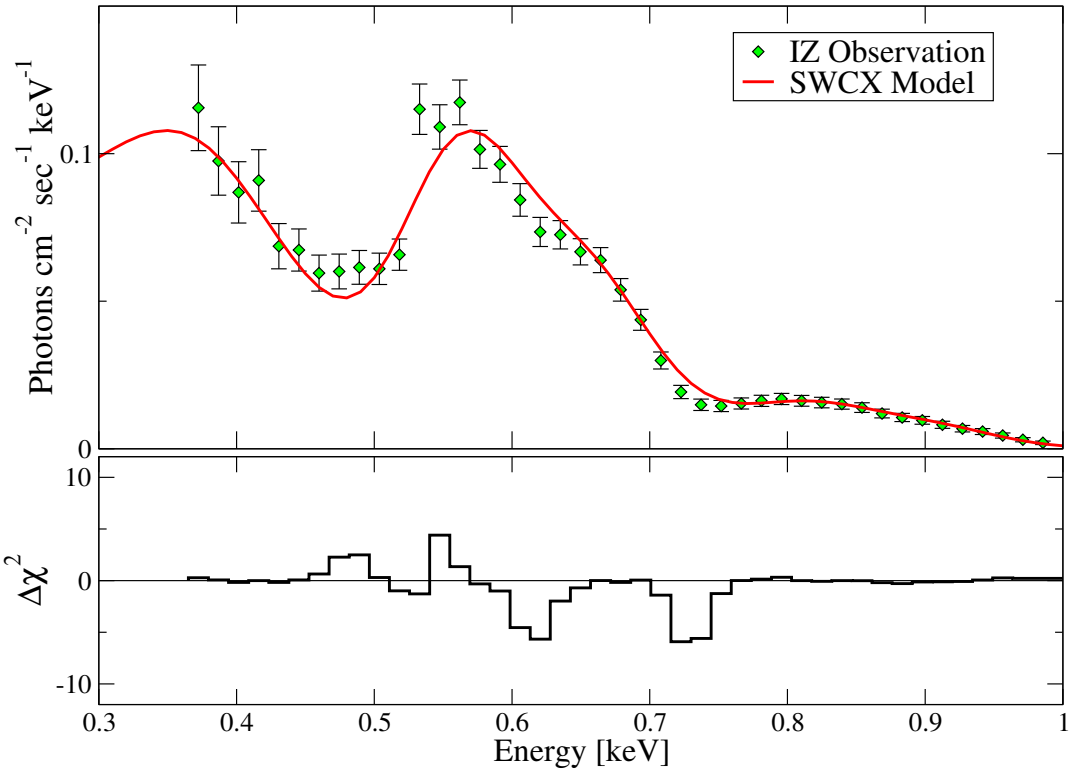

Fig. 5.4: Comparison between our CX model and the average background-corrected observations for comet Ikeya-Zhang and the χ^2 residuals ($\Delta\chi^2$) of the data-model comparison. Each observational spectrum has been grouped with a minimum of six counts per bin for proper statistics. Our model varies SW composition ratios until a best-fit is found. The resulting SW composition ratios for each model are detailed in Table 3.1.

Source	C^{6+}/C^{5+}	O^{7+}/O^{6+}	O^{8+}/O^{6+}
IZ	1.35	0.25	0.16
ACE	1.11 ± 0.44	0.14 ± 0.01	—
ISON	1.35	0.28	0.14
ACE	$1.18^{+0.80}_{-0.48}$	$0.25^{+0.12}_{-0.08}$	$0.09^{+0.19}_{-0.06}$
PanSTARRS	1.29	0.12	0.05
ACE	$1.09^{+0.62}_{-0.39}$	$0.22^{+0.13}_{-0.08}$	$0.08^{+0.14}_{-0.05}$

Table 5.2: A comparison between the model-calculated SW ion ratios and the average values observed by *ACE*. All calculated values are found to have an average uncertainty of ±20% and agree to the observational data within uncertainty, aside from IZ which was observed highly irregular solar activity. We note that agreement between *ACE* and PanSTARRS is inconclusive given the significant difference in heliospheric latitude between the two.

viding a more complete and physically accurate picture of the CX process in cometary atmospheres.

In addition to accurately modeling the cometary emissions, we compare our modeled SW composition results to contemporaneous composition ratios provided by *ACE*. A comparison of our model results of comet IZ to *ACE*, shown in Table 5.2, demonstrates an agreement within uncertainty for the C^{6+}/ C^{5+} ratio but not for O^{7+}/O^{6+}. The discrepancy may be attributable to the high solar activity we previously discussed cou-

pled with the non-isotropic nature of the SW emissions. In addition, SW conditions are known to differ significantly from Earth's observations at high heliospheric latitudes ($Lat_{\odot} > 20^{o}$) [3], and IZ was observed at a latitude of 26.42^{o}. We therefore find these comparisons to indicate our results are within the appropriate physical limits for the system, but direct comparison between *ACE* and IZ is inconclusive due to additional sources of uncertainty.

Our analysis of SW composition shows an above average amount of highly charged ions, such as O^{8+} and C^{6+}, with an decrease in their lower energy variants present at the cometary atmosphere. The heightened solar emissions would explain the high intensity detected from IZ and would also have a significant impact on the remaining emission mechanisms, making it a prime target for SF detection.

Comparison of Ikeya-Zhang to Jovian Disk

Spectral shapes are unique for different X-ray generating processes such as bremsstrahlung, scattering, or SWCX mechanisms. Analysis of the relative spectral shape of detected X-ray signals is broadly used to determine the physical mechanisms responsible for X-ray emission. We therefore compare the observed spectral intensity of IZ to detections of X-ray scattering from the Jovian disk as evidence of scattering above 1 keV in cometary atmospheres.

Measurements of Jovian X-ray emissions with *XMM-Newton* have previously been performed during a series of M-class solar flares [64, 65]. Accurate time and

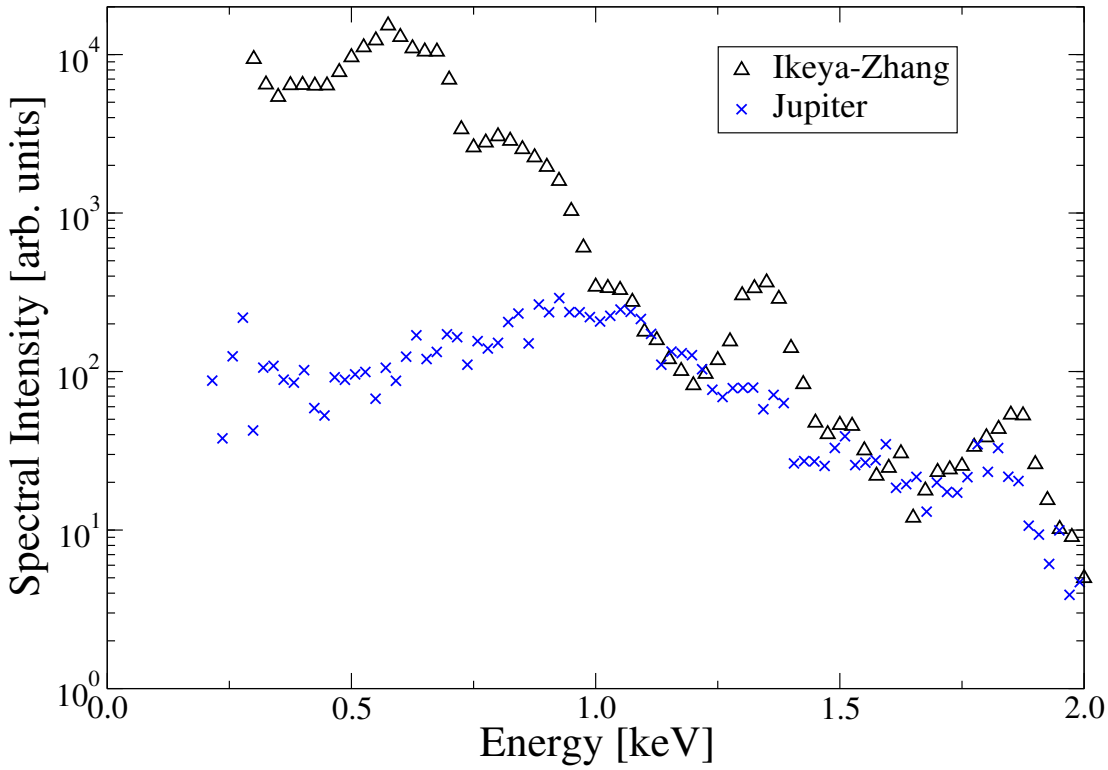

Fig. 5.5: Comparison of X-ray spectra from comet Ikeya-Zhang [10] and Jupiter [64], observed during solar X-ray flares. The data sets have been scaled to overlay each other in order to better visualize the strong similarity in spectral structure between the two astronomical objects at energies above 1 keV.

spectral correlation between the solar X-ray flares and disk X-ray emissions have been analyzed in detail [64], concluding that peaks observed above 1 keV were generated from the scattering of solar X-ray photons from Jupiter's outer atmosphere [64]. We can therefore infer a similarity between the production mechanisms within each system, namely scattering of solar X-rays, if we demonstrate a similarity in the general shape and peak structures observed from both the Jovian disk and comet IZ. Above 1 keV there are no significant resonant scattering or absorption cross section features for the primary scatterers present within the cometary and Jovian atmospheres, as shown in Fig. 4.2. We therefore assert that any similarities of spectral structure, which is defined as a similarity of relative intensities of important spectral features, are independent of atmospheric composition and would exclusively be attributed to relative intensities of the spectral features in the solar X-ray spectra.

Figure 5.5 shows the relative spectral intensities for Jupiter from *XMM* overlaid with the comet IZ data taken from *Chandra*, with both data sets corrected for the differences in effective areas of the two telescopes. The results show a strong similarity in overall spectral shape between the two objects at photon energies above 1 keV. Although each observation was taken during separate solar flares, the peak structures above 1 keV agree with regular features seen in observed solar flare spectra [56] and are common for average M-class solar flare activity [54, 55].

Differences between the IZ and Jupiter spectra near 1.35 keV may be a result of a difference in intensity of the Mg XI (2p–1s) emission line present in the solar

flare spectra during the Jupiter and IZ observations. The peak seen in both spectra at 1.85 keV may be a combination of scattered Si XIII (1.85 keV) X-ray emission line from the solar flare and Si K (1.74 keV) fluorescent emission by dust. Spectral differences below 1 keV are explained by the SWCX mechanism of cometary X-rays, which produces additional X-ray photons in the cometary spectrum that the Jovian disk spectrum would lack because it is produced entirely via SF.

As Jupiter disk emissions are shown to be a result of scattering, this strong agreement in spectral shapes above 1 keV leads us to consider that both spectra are produced via the same mechanism, the scattering of solar X-rays. Because both spectra were observed during solar X-ray flares, the similarity of the scattering mechanisms is even more evident.

Analysis of Gas Scattering Emissions

Motivated by our IZ-Jupiter comparison, we analyze the total contribution of gas scattering in the observed IZ spectrum. Figure 5.6 shows the theoretical spectral intensity of the SF cometary X-rays induced by the atmospheric gas together with the X-ray spectrum observed from comet IZ. We found reasonable agreement in the overall peak structures to our SF model at energies above 1 keV. The largest discrepancy occurs at ~1.35 keV where IZ shows a well-pronounced peak whereas our model does not. This discrepancy may be the result of utilizing an average solar X-ray emission spectrum to model our spectral intensities rather than utilizing direct observations.

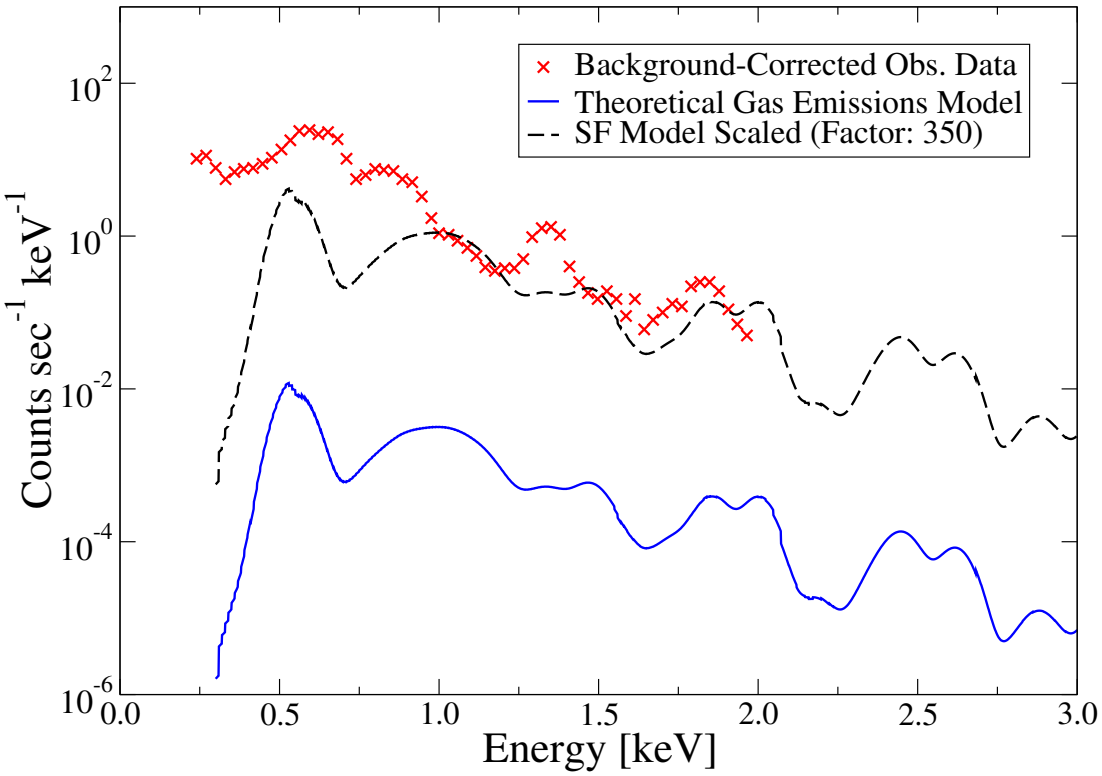

Fig. 5.6: Comparison between the spectral intensities of background-corrected observational data taken from *Chandra* (Xs) and our theorized scattering-fluorescence spectrum model induced exclusively from atmospheric gas (solid line) for Ikeya-Zhang. The dotted-line plot is the model scaled to match the observational intensities. We note the similarity in peak structure at energies greater than 1.5 keV.

Although the spectral shape of the theoretical gas scattering model agrees well with observations of IZ, the total intensity of the predicted SF spectrum above 1 keV is lower than the observed by a factor of ~350. This discrepancy is too great to be accounted for through uncertainties in our calculations or background corrections, and so we conclude that gas scattering of high-energy photons is not a significant source of cometary X-ray emissions given our model parameters.

Analysis of Nanoparticle Emissions

The presence of additional scatterers in the cometary atmosphere could explain a similarity of spectral shapes of the high-energy cometary emission and solar X-rays. Nevertheless, these particles should be inefficient in scattering of optical and infrared radiation. They should also be inefficient in fluorescence radiation as analysis of observed cometary X-ray emissions have shown that fluorescence from O and several lighter elements are a minor X-ray source in comet emissions less than 1 keV [5]. Nano-sized dust and ice particles would satisfy such conditions [5]. Nanoparticles as additional scatterers could significantly influence the intensity of the high-energy tail for cometary X-ray spectra and should therefore be analyzed in detail.

To investigate the role of nano-sized dust and ice particles, we incorporate the cometary dust density distributions from Fink and Rubin [38], as discussed in section 4.5. The comparison of the cometary X-ray emission contribution from nanodust to gas is shown in Fig. 5.1. Nanoparticle contributions to cometary X-ray emissions are 3–4

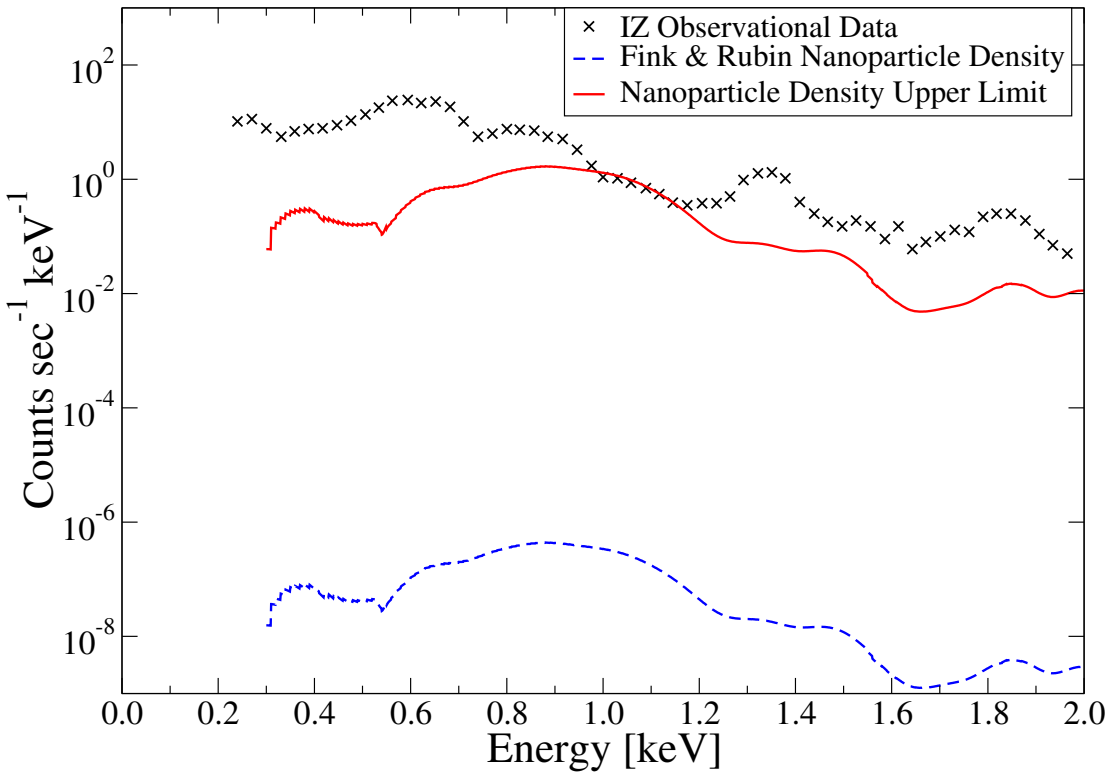

Fig. 5.7: A comparison of total spectral intensity contributions from nanoparticle scattering to observational data of Ikeya-Zhang (Xs). The Fink and Rubin [38] dust distribution represent an average dust density (dashed line), while the upper limit approximation (solid line) represents a hypothetical cometary atmosphere where nanoparticle dust and ice production rates are equal to gas production rates.

orders of magnitude lower than those from gas, indicating that nanoparticles have little impact at these densities on the overall emission spectrum.

As our results shown in Fig. 5.1 are based on data for dust and ice densities that are extrapolated from micron-sized particles down to nanoparticles, it is possible that nanoparticles, especially small ice particles, are more abundant than predicted by such a scaling technique. For example, the size-distribution density of small particles given by Eq. 4.12 may sharply increase with an α between 3–5 as particle radii become less than 100 nanometers [66, 67]. At the present time, there are no observations or consistent theories providing robust information on distributions of nano-sized dust and ice particles. We therefore investigate the upper limit of nanoparticle scattering by scaling nanoparticle emissions equal to the observed IZ emissions to extract maximum production rates and densities.

Figure 5.7 shows the observational data from IZ compared with the Fink & Rubin 2012 model and a maximum nanoparticle density model. Although the Fink & Rubin 2012 model cannot accurately represent the size distributions of nanoparticles, it may provide a general description of efficiency of X-ray scattering by small ice and dust particles. We note the disparity between the nanoparticle model and the observed spectrum at higher energies. This discrepancy can be attributed to the bias towards smaller scattering angles at higher energies from Mie approximations rather than spectral differences between observational and theoretical data [41]. The classical Mie model is known to be invalid for the scattering of high-energy photons because the wavelengths

of X-ray photons are comparable to the size of dust and ice nanoparticles and therefore the actual geometric shape of the nanoparticles plays an important role.

If the actual complicated geometry of dust and ice nanoparticles were taken into account and a more accurate scattering theory were incorporated, such as quantum mechanical calculations with simplified electronic wave functions of nano-sized grains/particles or classical discrete dipole approximation modeling for aggregate dust particles [68], we might obtain the theoretical spectral shape of scattered X-rays that provide a stronger agreement to those observed. However, such calculations are beyond the scope of our investigations.

In addition to the discrepancies with the spectral shape, we note that the required nanoparticle densities to produce such X-ray emissions are significantly higher than the observed density of micron-sized dust and ice particles. In order for the resulting increase in scattering intensity shown in Fig. 5.7 to be exclusively from nanoparticles, their mass production rate over a 1–10 nm radii range must be equal to the gas mass-production rate.

Dust production rates can be significantly higher than gas production rates. Although it is possible that nanoparticles may be more abundant in the cometary atmosphere than previously theorized, we assert that a more realistic model should treat production of nano-sized particles between 1–10 nm consistently with distributions of larger grains using results of previous observations, such as data from McDonnell et al. [51].

Analysis of Dust and Ice Emissions

As we have shown that nanoparticle scattering could not be responsible for the high energy spectral features from IZ with currently accepted physical parameters, we instead consider possible contributions from dust grains of all sizes. We extend the upper limit of our dust equations from Sect. 4.5 to an upper limit grain radius of 1 cm. The mass loss rate is held fixed and is now distributed over the wider range of particles to ensure the physical constraints of the system are preserved. By modifying our dust radii, we now must calculate the cross sections for all particles over the radii range. Rather than derive the the cross section for every grain size, we instead develop a relationship to describe cross section as a function of grain radius.

To begin our derivation, we consider a porous, optically thin dust grain that will approximate a small grain particle. We assume summation over all possible grain configurations will produce an isotropic shape as its average, and so we define the total particle density as

$$N_a(a) = \frac{4\pi}{3} a^3 n_a, \tag{5.8}$$

where a is the grain radius and n_a is the atomic, or molecular, particle density within the grain. Assuming the particle is porous enough where each atom or molecule may be considered non-interacting with any other, the total cross section Σ_{small} should equal:

$$\Sigma_{small}(a) = N_a(a)\sigma_p = \frac{4\pi}{3} a^3 n_a \sigma_p, \tag{5.9}$$

where σ_p is the cross section of an individual atom or molecule. A comparison of calculated values from this equation to those found from Mie scattering for particles 1 nm show strong agreement, and so we use Eq. 5.9 as our small cross section approximation.

To calculate the upper limit of our cross section range, we recall that for a macroscopic, spherical particle, the cross section may be defined as

$$\Sigma_{large}(a) = 2\pi a^2, \tag{5.10}$$

which we will use as our upper limit. We then define that our calculated cross section should evolve over this range based on the equation

$$\Sigma_{total}(a) = \frac{\Sigma_{small}(a)\Sigma_{large}(a)}{\Sigma_{small}(a) + \Sigma_{large}(a)}. \tag{5.11}$$

After inputting our values for Σ_{small} and Σ_{large}, we then simplify Eq. 5.11 and return

$$\Sigma_{total}(a) = \frac{\frac{4}{3}\pi n_a \sigma_p a^3}{1 + \frac{2}{3} n_a \sigma_p a} \tag{5.12}$$

as our final expression for cross section dependence as a function of grain size. Again, it is worth stressing that the main purpose of this equation is to understand the cross section as a function of grain size and not to calculate cross sections to high accuracy. With this dependence in-hand, we may now utilize theoretically and experimentally calculated cross sections and apply our relationship to approximate the cross sections for our model over the entire grain radii range. This modeling should provide an approximate spectral intensity generated due to dust and ice particle scattering within a

cometary atmosphere.

Applying the revised dust scattering model to comet IZ produces the result shown in Fig. 5.8. Surprisingly, the additional amount of dust scatterers provides a significant boost to the total scattering emissions, ultimately surpassing gas scattering emissions and equalling the observed intensity seen from IZ at over the 1.0–2.0 keV energy range. The observed emission peak at 1.85 keV agrees well with our scattering model, providing further evidence that this spectral feature is a by-product of scattering and not CX.

Despite the agreement between the two data sets, we note the significant discrepancy between the observed spectrum and the modeled scattering spectrum at 1.35 keV and at 1.75 keV. The difference at 1.75 keV is likely due to detector contamination from the Si K absorption edge line present in the ACIS-S detector and does not reflect a true difference between theory and experiment. However, the difference at 1.35 keV is indeed physical and may be a result of two possibilities:

1. Scattering of the Mg XI (2p–1s) emission line present in the solar flare spectra. This line has been seen in previous solar flare observations [56], and we believe IZ to have been observed during solar flare activity.

2. CX emissions coming from from Mg XII ions. Although these ions have not been directly observed and are unlikely to be present in SW due to freezing-in temperatures, exotic solar conditions may produce these ions in enough abundance to be detectable through spectral analysis of CX emissions. This would also be in

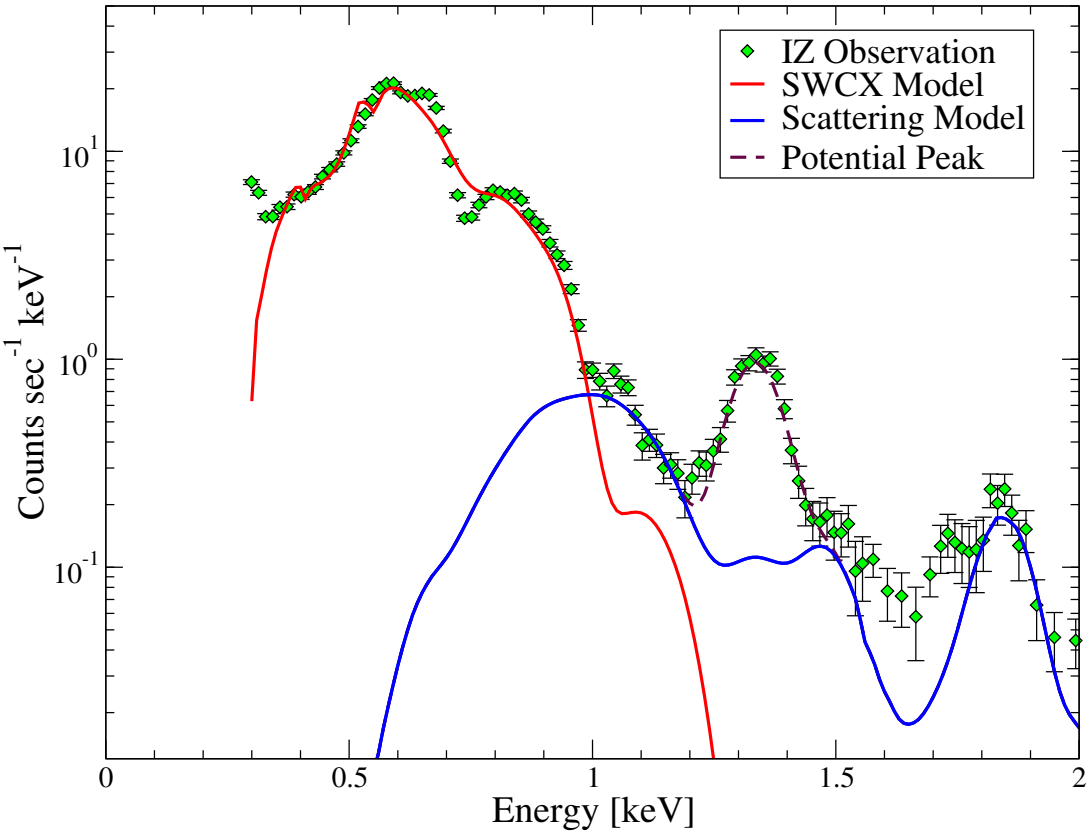

Fig. 5.8: A comparison of the approximated total spectral intensity contributions from dust and ice particle scattering to observational data of Ikeya-Zhang. The model emission includes dust contribution from all grain radii. The potential peak shown may possibly be from either CX or scattering and is currently unclear with is the most likely source.

keeping with the Jupiter-IZ comparison where Jupiter scattered emissions also did show at a peak at 1.35 keV.

Given the limited dataset on this spectral feature, it is impossible to provide a conclusive answer to its origin. Nonetheless, our results help limit possible explanations while also providing strong evidence that the higher emission feature at 1.85 keV is indeed from scattering. If true, properties of dust and ice particles within cometary atmospheres may be obtained by modeling spectral intensity emissions over the 1.0–2.0 keV energy range. Further improvements such as the introduction of accurate dust grain morphology in cross section analysis should be incorporated into our scattering model to more accurately quantify dust density distributions as well as grain radii dependence.

5.4 PanSTARRS

Prior to the *Chandra* observation of comet PanSTARRS, infrared observations of the comet indicated an average dust-to-gas emission ratio of ~4 [69]. Therefore, there was much speculation if its high dust-to-gas ratio would significantly affect its X-ray CX emission intensity as it is more favorable to produce Auger electrons instead of X-rays when undergoing CX with dust particles [60, 70, 71]. We therefore make sure to note any X-ray emission irregularities within our results and, if so, their possibility of being due to dust particles.

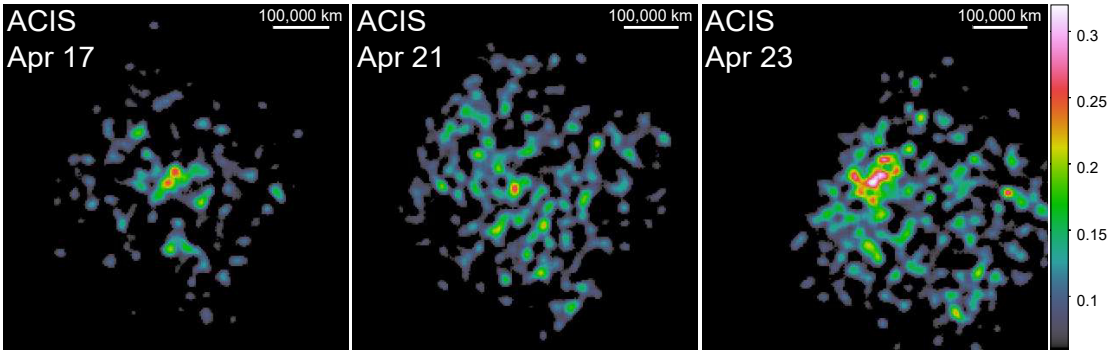

Fig. 5.9: *Chandra*/ACIS-S observations of comet PanSTARRS. The images are binned to include all 0.3–1.1 keV photon events, exposure corrected, on the same linear scale, and smoothed with a 5×5 pixel Gaussian filter. Our results show fluctuations in X-ray emission intensity, and the overall morphology is highly non-uniform.

Morphology

We present the ACIS observation images of comet PanSTARRS in Figure 5.9. All images have been corrected for differences in exposure time and are normalized to the same linear scale. These images show a constant intensity in X-ray emissions in all the observations, as we expect given the constant cometary dust/gas emission rates and SW conditions observed at the time of our observations. We also find that the overall morphology is highly non-uniform, and so we conclude that PanSTARRS was collisionally thin during its observations. This is likely a result of the high dust density present in the cometary atmosphere as dust particles are significantly less efficient in CX X-ray production than molecular gas [60, 70, 71].

Emission Spectrum

Utilizing our CX model, we are able to successfully characterize PanSTARRS' spectrum up to 1.0 keV without making any adjustments to our CX scenario, as shown in Fig. 5.10. Above 1.0 keV, the uncertainty in the observations becomes too great to distinguish between noise and emission peaks. For PanSTARRS, which has 30 dof, we find $\chi^2_R = 1.2$ for the 0.35–1.00 keV range. Since no features were observed above 1.00 keV, SF emission modeling was not performed.

A comparison of our model results to *ACE*, shown in Table 5.2, demonstrate an agreement within uncertainty for all observations. Analysis of SW composition through the use of our model shows a lower than average amount of highly charged ions, such as O^{8+} and Ne^{9+}, with an increase in their lower energy variants, like O^{6+} and Ne^{8+}. This result agrees with our previous assessment that PanSTARRS was observed at fast, polar SW. Beyond this irregularity, PanSTARRS' spectrum possesses no additional traits that would classify it different from any other comet X-ray spectrum.

Although we cannot infer from our spectral analysis how PanSTARRS' large dust quantities may have impacted other emissions mechanisms present within the cometary spectra, our results indicate that it had little to no observable impact on the comet's CX X-ray emissions. As such, any differences present are more likely attributed to the SW flux density and ionization state at the time of observation.

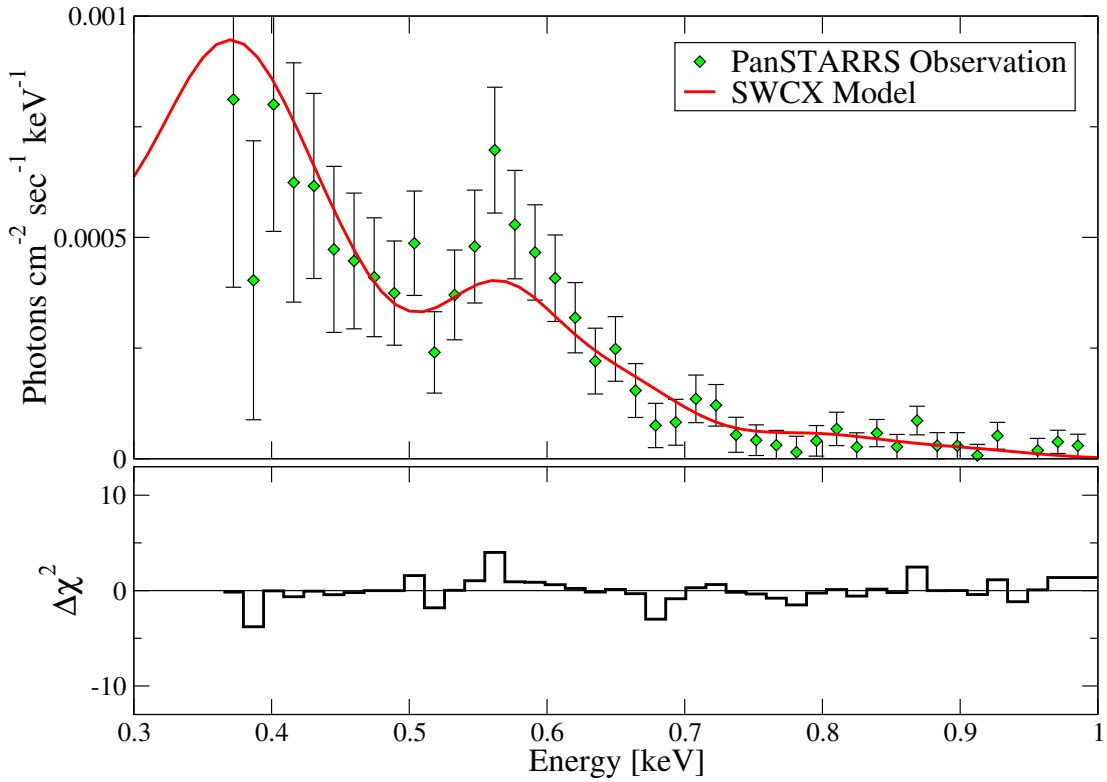

Fig. 5.10: Comparison between our CX model and the average background-corrected observations for comet PanSTARRS and the χ^2 residuals ($\Delta\chi^2$) of the data-model comparison. Each observational spectrum has been grouped with a minimum of six counts per bin for proper statistics. Our model varies SW composition ratios until a best-fit is found. The resulting SW composition ratios for each model are detailed in Table 3.1.

5.5 ISON

Despite being one of the brightest comets in recent years, the *Chandra* observations of ISON that we analyze were taken slightly prior to ISON's drastic increase in gas production rate starting on 2013 November 13. Fluctuations in SW speeds, as confirmed by *ACE*, and several M-class solar flares, as reported by *GOES*, were also observed during ISON's *Chandra* visits. These highly volatile SW conditions may significantly impact ISON's emission spectra, similar to what we saw for IZ.

Morphology

The ISON observations were unique as it was the first time HRC observations of a comet were performed in conjunction with ACIS observations. The extracted ACIS and HRC images for the three ISON observations are shown in Figure 5.11. Each image set, either from ACIS or HRC, has been corrected for differences in exposure time and has been normalized to the same linear scale. The ACIS images demonstrate the expected paraboloid morphology of a collisionally thick case, while the HRC observations depict a more non-uniform emission typical of a collisionally thin case. Given that HRC is more sensitive to soft X-rays than ACIS, this result may indicate that the soft X-ray emissions are due to CX emissions from lighter SW ions with smaller cross sections, such as He^{2+}, than the SW ions that emit hard X-rays, such as C^{6+} and O^{8+}. The reduction in cross section allows for deeper penetration into the cometary atmosphere, and it may be substantial enough to generate the difference in these image sets.

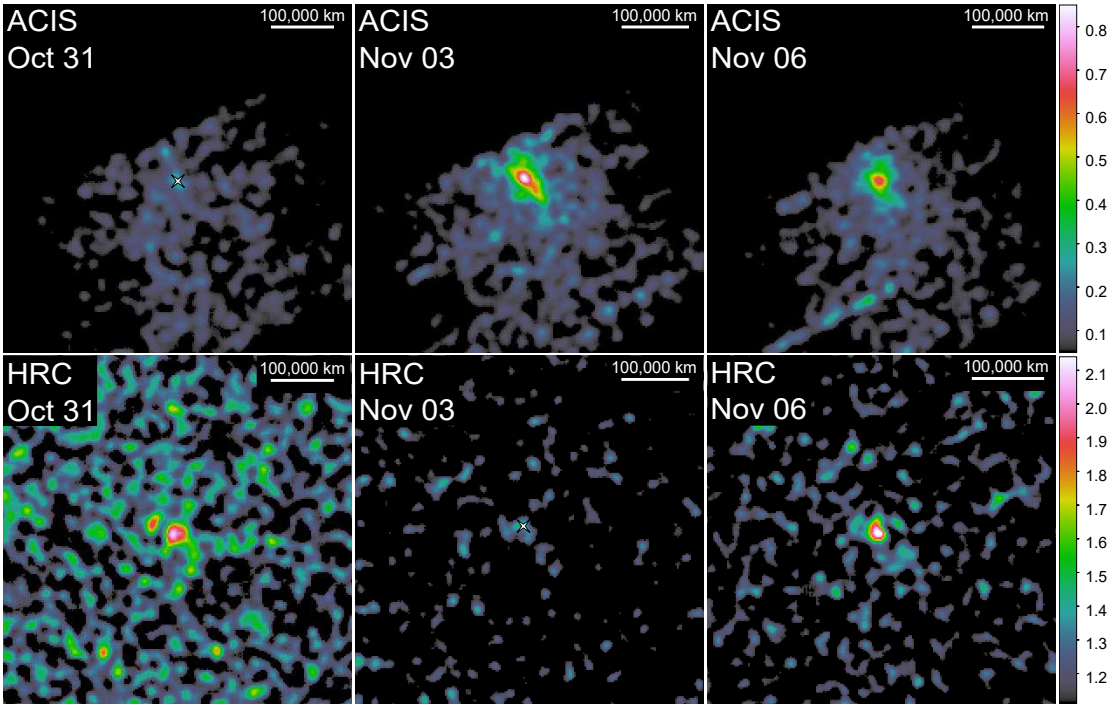

Fig. 5.11: *Chandra*/ACIS-S and HRC-I observations of comet ISON. Each set of images (either ACIS or HRC) are exposure corrected, shown on a linear scale, and smoothed with a 5×5 pixel Gaussian filter. ACIS images are also binned to include all 0.3–2.0 keV photon events. The images show a "see-saw" effect between the soft X-ray HRC observations and hard X-ray ACIS observations where an increase of intensity in HRC correlates to a decrease in ACIS, and vice versa. This result also correlates to fluctuations in SW speed between October 31 and November 03 as seen via *ACE*.

It is also possible that the soft X-ray emissions from ISON are from a different emission mechanism that would not produce the same morphology, such as scattering or fluorescence.

The ISON image sets also demonstrate significant fluctuation in the cometary emission intensity over time and a "see-saw" in intensity between the soft X-ray HRC observations and the hard X-ray ACIS observations, most notably seen on the October 31 and November 03 visits. These intensity fluctuations correlate with increases in SW speed as documented by *ACE*, where the maximum SW speed was recorded November 03. Such an association between SW and cometary emission intensity is predicted by our CX model as SW speed fluctuations indicate fluctuations in SW ion freeze-in temperatures [12]. Such temperature changes shift the SW charge state distribution, producing a varying average cometary emission energy based on our normalized photon emission yield function $P_{k,l}^{(j)}(\hbar\omega_j)$. As we see a similar shifting of the average cometary emission energy, we therefore assert that CX emissions are the dominant cometary emission mechanism in the soft X-ray region, a fact that will become important in our discussion in Section 5.8.

Emission Spectrum

Using the ACIS observations and applying the same method as done for PanSTARRS, we are able to model ISON's spectrum as CX below 1 keV and extract SW composition ratios as shown in Fig. 5.12. For ISON, the $\chi_R^2 = 1.1$ over the 0.35–1.00 keV range for

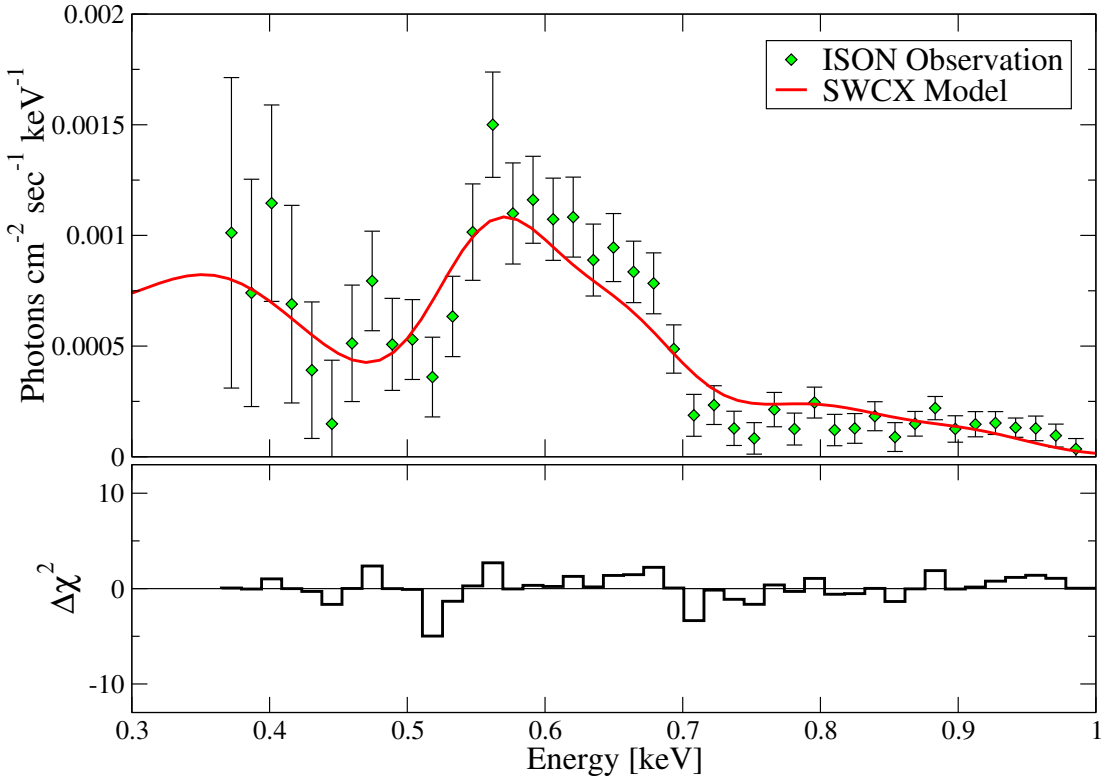

Fig. 5.12: Comparison between our CX model and the average background-corrected observations for comet ISON and the χ^2 residuals ($\Delta\chi^2$) of the data-model comparison. Each observational spectrum has been grouped with a minimum of six counts per bin for proper statistics. Our model varies SW composition ratios until a best-fit is found. The resulting SW composition ratios for each model are detailed in Table 3.1.

32 dof. ISON's ratios, as shown in Table 5.2, confirm the above average SW speed with an overabundance of highly charged SW ions, like O^{8+} and Ne^{9+}, that produces a distinct plateau in the spectrum from 0.75–1.00 keV. The O^{7+} ratio is twice that seen from PanSTARRS, best visualized via the emission peak at 0.6 keV.

In addition to these results, ISON exhibits some possible peak structures in its emission spectrum at energies above 1 keV: one peak at 1.35 keV and another at 1.85 keV, as seen in Figure 2.3. Such peaks have been previously seen in *Chandra*'s observations of comet IZ, as discussed in Sect. 5.3. As these peaks are not explained with our CX model, we therefore explore SF as a possible emission source.

As we did for IZ, we model SF emission spectra for ISON and compare our results to the observational data. Similar to IZ, the contributions from fluorescence, gas scattering, and nanoparticle scattering are all several orders of magnitude less than the observed spectrum, and so we find it unlikely that these three sources had any noticeable impact on the emission intensity. We therefore move on to analyzing total dust and ice scattering contributions.

Using the total dust scattering model we developed in Sect. 5.3, we model the total dust and ice scattering contributions for comet ISON and plot the results in Fig. 5.13. Our results show that the modeled spectrum is one order of magnitude lower in spectral intensity than what we observe from the comet, even after accounting for the the total dust scattering contributions. This result disagrees with our assessment of comet IZ which found excellent spectral agreement above 1 keV with the dust scattering

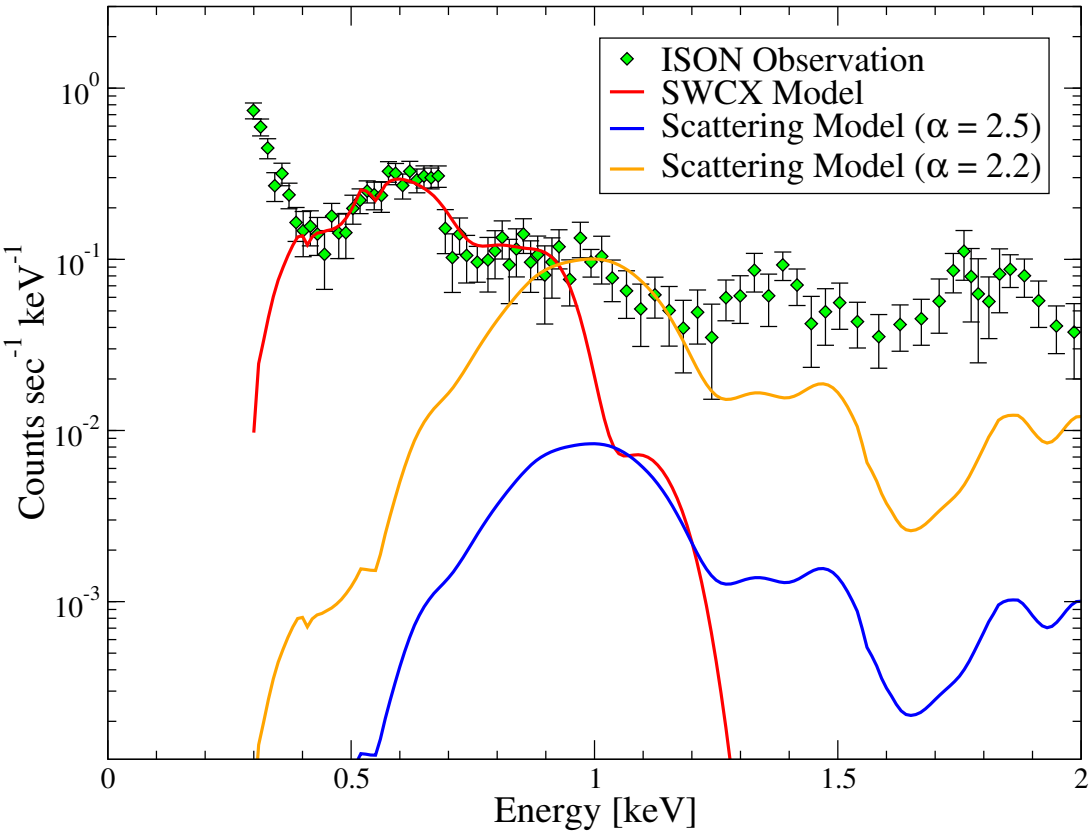

Fig. 5.13: A comparison of the approximated total spectral intensity contributions from dust and ice particle scattering to observational data of ISON. The model emission includes dust contribution from all grain radii. Each scattering model is calculated with a different grain radii dependece α.

model. Such a disagreement may indicate a different primary emission mechanism for ISON above 1 keV. However, it is unlikely for there to be a primary mechanism over the 1–2 keV energy that we have not already discussed, and all previous mechanisms were found to be lacking in intensity or too exotic to be considered probable. We therefore return to the dust scattering and note that it is based on the grain size a dependence of

$$n(a) \sim a^{-\alpha}, \tag{5.13}$$

where α is set to 2.5 for our model. Previous, independent dust modeling analysis have shown that average grain size dependence for diffuse system is equal to 2.5 [38]. However, such a relationship is dependent on various factors of the system, including: comet size, jet streams presence, jet stream locations, comet-Sun distance, comet composition, and comet origin. It is therefore possible that the dust relationship was different for ISON, producing a higher intensity scattering emission. We therefore modify our dust scattering equation to allow grain size dependence over a range of values found to be physically viable for a cometary system [37, 38].

Adjusting the grain size dependence over a range of 2.0–3.0, we find an agreement in intensity between the observation and our model over the 1.0–1.25 keV energy range for an α set to 2.2. The resulting comparison plot is shown in Fig. 5.13. Unfortunately, the modeled spectrum diverges from the observed spectrum at higher energies and does not produce a good fit. Given the limitations of both the X-ray solar spectrum model and the dust scattering model, it is possible this divergence is due to our

approximations and is not reflective of a physically relevant result. We therefore can only conclude that the ISON spectrum cannot be accurately modeled at higher energies using average physical parameters for both the solar spectrum and cometary dust and ice density distributions. However, we have shown that dust scattering can produce total intensity emissions equal to observational data and, given our analysis of the other most viable emission mechanisms in this energy range, dust scattering appears to be the most probable emission source.

5.6 Miscellaneous Comets

In addition to the three comets already discussed, we analyze four more comets. These comets are selected as previous analysis of each has been performed [10], and each comet demonstrates average emission rates as well as negligible emissions above 1 keV. As these comets better represent an average cometary emission spectra, we therefore investigate SF emissions to determine the probability of detection for a typical *Chandra* observation.

Our models are compared to observational spectrum and are shown in Fig. 5.14. The results clearly show that SF emissions are several orders of magnitude lower than the typical *Chandra* background count rates. We also note that the background rates fluctuate between $10^{-(0-2)}$ counts sec^{-1} keV^{-1} depending on the viewing angle, SW outflow rates, and *Chandra*'s effective area rate at the time of observation. As the average SF emissions are two orders of magnitude less than the background emissions,

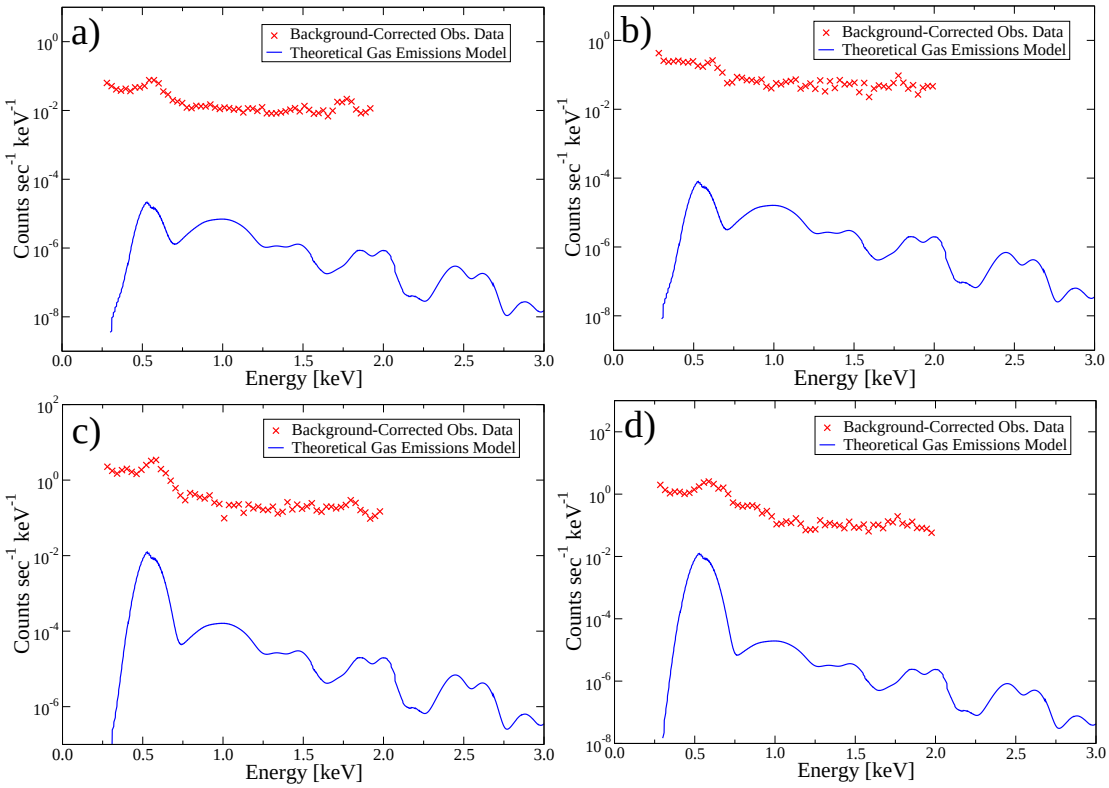

Fig. 5.14: Comparison between the spectral intensities of background-corrected observational data taken from *Chandra* (Xs) and our theorized scattering-fluorescence spectrum model induced entirely from atmospheric gas (solid line) for the following comets: a) 8P, b) Encke, c) LS4, d) MH.

we conclude that one of the following cases must exist for SF emission detection: high solar X-ray emissions (like the rates found during solar flares), abnormally high gas and dust outflow rates from the comet, favorable geometry for the observation, or a combination of these possibilities.

Examples of the outlined situations are shown for the IZ and ISON observations, both of which occurred during high solar flare activity and therefore allowed us to properly assess SF emissions. However, our analysis clearly shows that these cases are exotic as the average cometary SF emission are unlikely to be detected due to high background count rates.

5.7 Universality of Observed Cometary Spectra

We have shown throughout this chapter that the presence of cometary X-ray emissions is a common occurrence. Although spectral shape may vary depending on both the SW and cometary atmospheric conditions, X-ray emissions are frequently observed at high signal-to-noise ratios from any comet nearing its perihelion with the Sun. In addition, we notice similarity in emission peak structure from all comets over the 0.3–1.0 keV energy range. Due to the consistent spectral structure observed, we postulate that a universal cometary emission spectrum may be generated through the averaging of all available cometary X-ray observations [72]. As emissions over the 0.3–1.0 keV energy range have been shown be dominated by CX through our prior analysis, such a universal spectrum would provide additional insight into SW composition ratio fluctuations via

comparison in spectral shape to cometary observations. As we have already compiled a database of cometary spectra for our prior work, we set forth on development of a universal cometary emission spectra from observational data.

To begin, we return to the *Chandra Database Archive* to collect all available cometary observations for use in our analysis. In total, 10 comets are found in the archive that were all observed with ACIS-S in vfaint mode using the S3 chip as the aimpoint in drift-scan mode. Although additional comets are available for use, they all use the LETGS instrument for observations which was previously found inadequate for cometary observations due to the distended nature of the object. We extract all emission spectra using the procedure outlined in Chapter 2, ensuring to correct for the different effective area for each observation. We then normalize all spectra over the 0.35–1.50 keV energy range as this will include the majority of the total observed intensity for each selected comet while also avoiding any contamination issues from the carbon K-shell at 0.284 keV and Si K-shell at 1.75 keV. Each result is then interpolated and averaged together with all other spectra to produce a universal cometary emission spectrum.

Prior to comparing our universal cometary emission spectrum to observation data, we first fit the spectrum with our CX model to extract SW composition results. As our universal spectrum should be representative of average physical parameters for cometary emissions, we expect our SW composition results to reflect an average composition ratio. Fitting our CX model and extracting SW composition, we find that all

Ion	Avg. Ratio[12]	Model Ratio	Ion	Avg. Ratio[12]	Model Ratio
C^{6+}	0.318	0.310	O^{8+}	0.070	0.060
C^{5+}	0.210	0.210	O^{7+}	0.200	0.240
N^{7+}	0.006	0.008	O^{6+}	0.730	0.700
N^{6+}	0.058	0.052	Ne^{9+}	0.004	0.005
N^{5+}	0.065	0.069	Ne^{8+}	0.084	0.091

Table 5.3: Average slow solar wind ratios compared to SW ratios extracted from the universal cometary X-ray spectrum. All ratios are normalized with respect to the total solar wind oxygen composition.

ratios agree with the average SW ratios to within 5% [72]. See Table 5.3 for a comparison of our extracted results to average SW composition. We therefore conclude that the universal cometary emission spectrum is consistent with our initial hypothesis. In addition, our spectrum is therefore valid as a universal SWCX emission model for any diffuse astrophysical source emitting CX as the overall structure of the spectrum is largely independent of the source. Our universal spectrum would therefore not only work for comets but also planets, asteroids, or any local deposits of dust/gas particles emitting X-rays due to CX.

Having established our universal spectrum to be consistent with physically expected results, we present the average cometary emission spectrum compared to observations of several comets in Fig. 5.15. Our comparisons indicate that the average

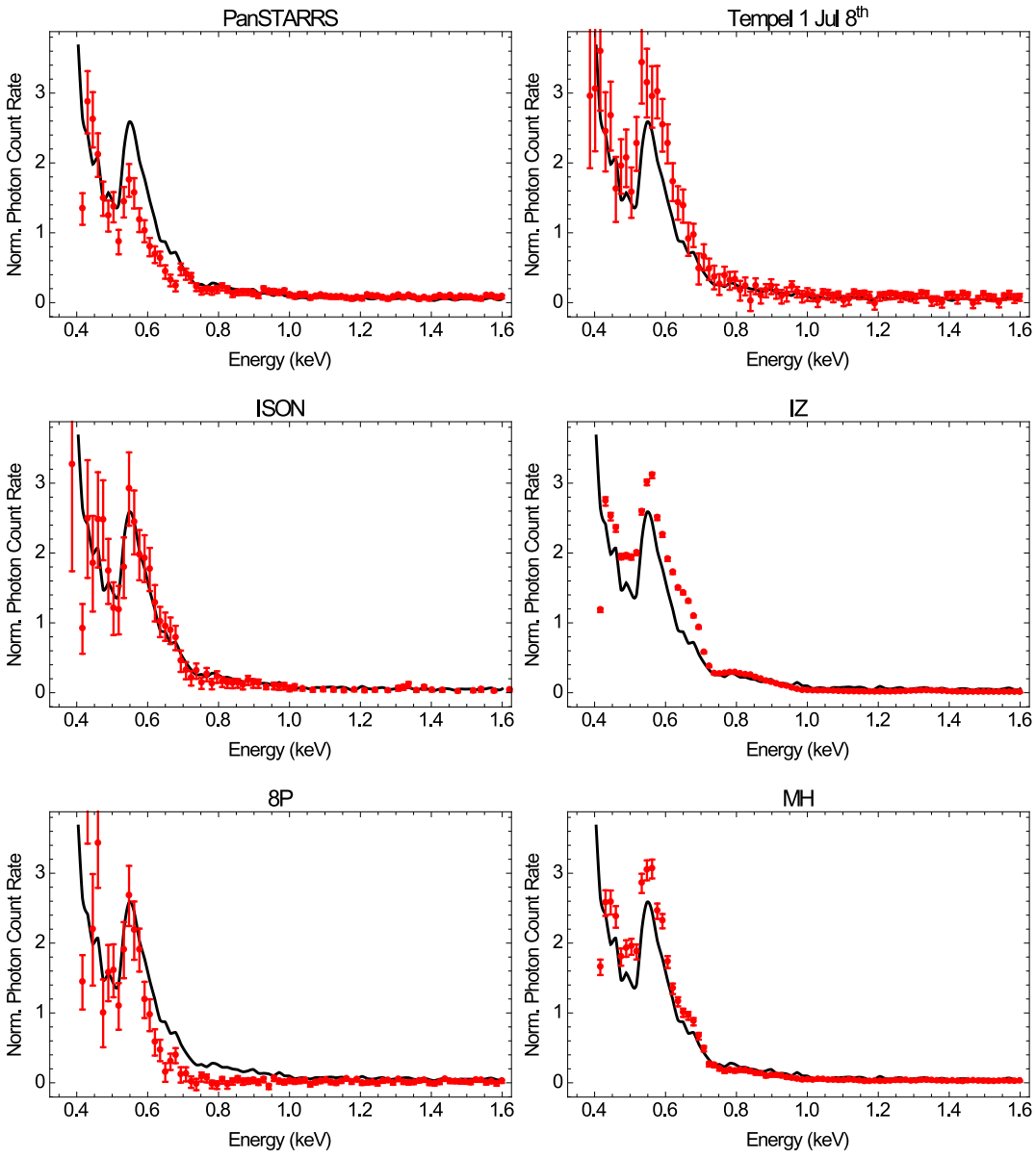

Fig. 5.15: Comparison between the universal emission spectrum and several comets. All spectra have been converted to physical units and normalized over the 0.35–1.50 keV energy range. Differences between the universal curve the cometary spectra indicate differences in SW composition, with observations below the curve indicating below average SW activity and observations above the curve indicating heightened SW activity.

spectrum agrees well to observational data for X-ray emissions up to 0.5 keV. Examination of higher energy emissions shows clear differences between our spectrum and observed data for the majority of comets, with discrepancies seen both above and below the universal curve depending on the comet analyzed. Emissions generated above 0.5 keV are primarily due to exotic emissions from H-like SW ions that may fluctuate significantly in densities over time. It therefore is logical that such variations between average emissions and observed rates would be observed as they are tied to SW composition during the time of observation, with observations below the curve indicating below average SW activity and observations above the curve indicating heightened SW activity [72]. Our comparison between the average and observed spectra provides us with an immediate understanding of SW conditions at the comet during the *Chandra* observations prior to our thorough CX analysis, giving us quick insight into expected results.

Beyond the ease of access that our universal spectrum provides to information on SW activity, we note some inconsistencies within our results. When comparing our results to observations, we notice irregularities with a few comets, notably IZ and ISON, that dip below the average emission spectrum at energies greater than 1.0 keV despite being previously shown as abnormally bright comets. These deficiencies are a by-product of two key issues:

1. The selected normalization range includes the peak structure at 1.35 keV present in both comets IZ and ISON, significantly altering the way the normalization is

weighted over the 0.3–1.5 keV energy range

2. The high intensity comets have an above average signal-to-noise ratio, producing a more prominent high energy tail before being overwhelmed by background emissions. As less intense comets approach their noise floor of signal intensity faster than high intensity observations, normalization between different sets of comets will again provide different weighting for the spectra.

It is clear that inconsistent weighting of the observation spectra when calculating the universal curve presents issues when irregular spectra with high energy emissions are analyzed. Future analysis on a universal cometary spectrum may want to instead normalize over both a soft X-ray band and a hard X-ray band when comparing soft and hard X-ray emissions, respectively, to reduce issues in normalization weighting. In addition, a universal spectrum for high SW activity may also be developed that will better fit these exotic cases. Such a spectrum would require further observations to be taken during such SW conditions, as the current sample pool is too low for statistically relevant count rates.

Despite some issues present with exotic emissions, our results show a universal emission spectrum that is able to accurately reproduce soft X-ray features while also indicating SW conditions during the observation without the need for SW dynamical modeling or CX analysis. These results provide a quick, visual indication of SW conditions for the observation that may be used in conjunction with any diffuse astrophysical system emitting via CX, including comets, planets, and dust/ice clouds.

5.8 Potential Soft X-Ray Emissions from ACIS

While examining the ACIS spectra from ISON, we found a peak-like feature located at 0.2 keV. This feature was also found in the PanSTARRS observations, but with a lower relative spectral intensity. After removing the portion of the spectra caused by the carbon K-shell detector contamination at 0.284 keV, we plot the resulting emission spectra for each of the three ISON visits in Figure 5.16. Our plots show a soft X-ray region at 0.2 keV that the detector is sensitive to after our corrections, even showing fluctuations that agree with the soft X-ray emission fluctuations detected by HRC (see Figure 5.11). The overall shape of this feature is likely due to the ACIS effective area function abruptly decaying toward zero at 0.18 keV and is not due to any specific emission line. Also, the fluctuations between the visits exceed the spectral intensity uncertainty in this region, which is 0.08 counts s^{-1} keV^{-1}, and so we believe these features to be physical.

Based on our HRC results from Sect. 5.5, we assume CX emissions to be the most likely cause of this feature. We therefore extend our CX model down to this soft X-ray region and plot the results with the observational data. See the dotted lines in Figure 5.17 for our predicted CX model for each observation. Calculation of a unique solution of SW ratios required to produce such intensities is not possible due to the abundance of over 200 unique lines from over 15 different SW ion types that fall within ACIS' resolution of this soft X-ray feature. We therefore choose to leave our model at average SW abundances in this region. We note that fixing these parameters produces no difference in the spectral fit over the 0.3–1.0 keV energy range.

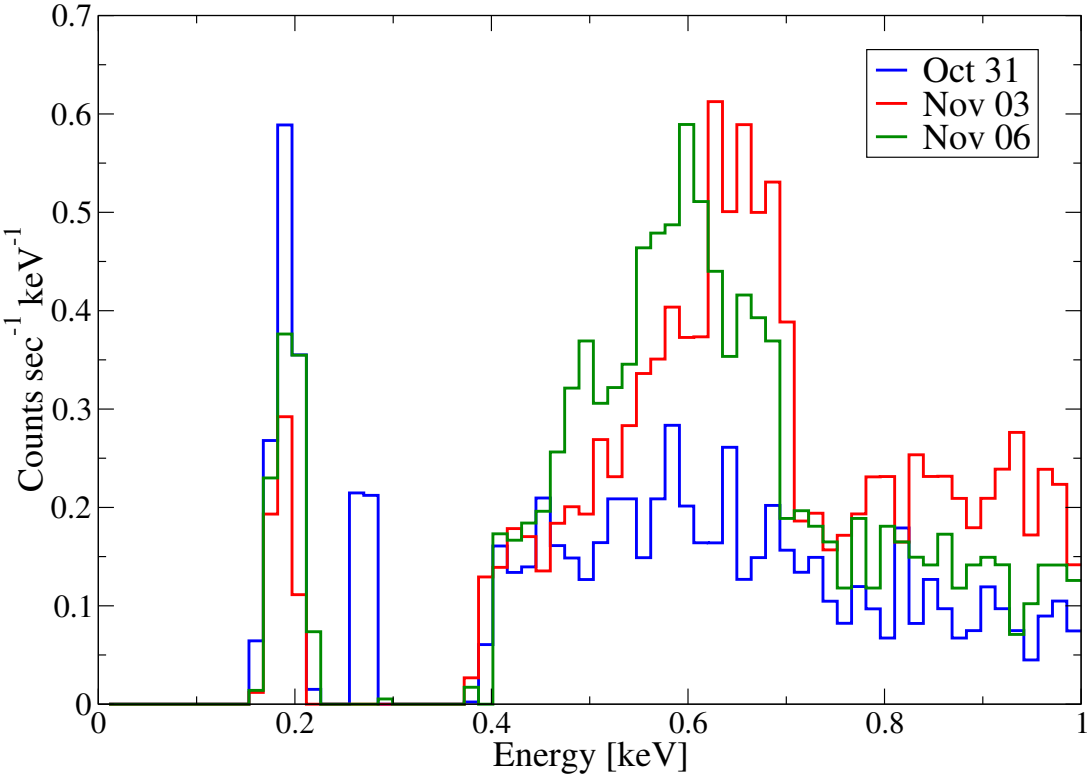

Fig. 5.16: ACIS spectral intensity for each observation of comet ISON. All detector contamination from the carbon K-shell at 0.284 keV has been removed from the spectra. The observed spectral feature at 0.2 keV has the the same fluctuation in intensity that is observed from the HRC observations and exceeds the average spectral intensity uncertainty in this region, and so we conclude that this feature is physical. Possible origins of this spectral feature are discussed in Section 5.8.

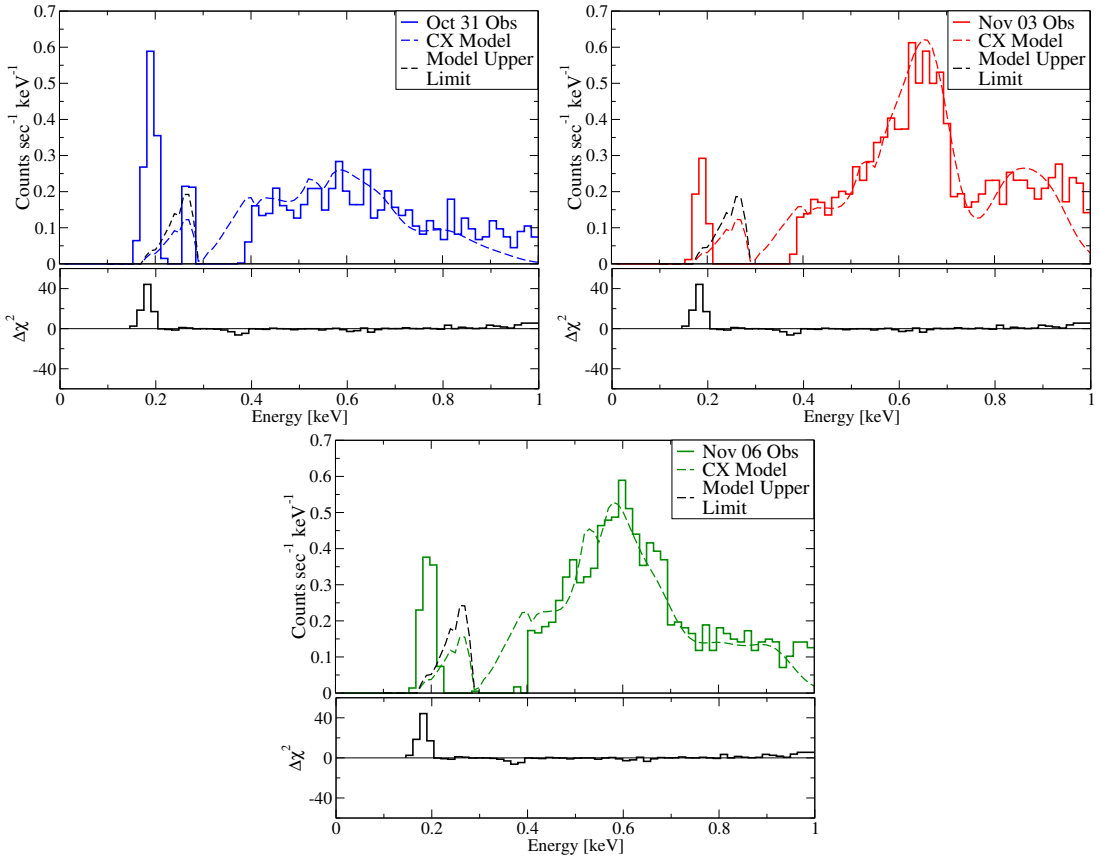

Fig. 5.17: ACIS spectral intensity for each observation of comet ISON (solid lines) and its respective modeled CX using average SW compositions (dotted colored lines). All detector contamination from the carbon K-shell at 0.284 keV has been removed from the spectra. Despite the excellent agreement above 0.4 keV, our model fails to match the shape and intensity of the soft X-ray spectral feature. We also calculate an upper limit to soft X-ray CX emissions by accounting for sequential CX events (dotted black lines), and our results show these additions to be insufficient to equal the observed soft X-ray intensities.

Our results show that our average CX model is not capable of producing the necessary intensity to match the observations for either the ISON emissions or the PanSTARRS emissions, which are not shown. Furthermore, the SW abundances that our model would demand to match these features in intensity far exceed their physical boundaries, with most abundances requiring an increase by an order of magnitude. Although such exotic SW compositions are not impossible given its constantly fluctuating nature, the consistent presence of these soft X-ray features during both fast and slow SW indicate these should be generated under average SW conditions.

Although our current CX model does not agree with the soft X-ray intensities detected, we only consider a single electron capture event per incoming SW ion. Sequential capture events may occur for an ion if the cometary atmosphere is collisionally thick, increasing the amount of soft X-rays emitted from the system as the ion charge state decreases ($O^{8+} \rightarrow O^{7+} \rightarrow O^{6+} \rightarrow$ ...). We therefore modify our CX model to include these sequential capture events per ion as it may solve our soft X-ray intensity deficit.

For our analysis, we calculate an upper limit on the increase to soft X-ray CX emissions from sequential capture events by assuming all SW ions are neutralized through interaction with the cometary atmosphere. Our results are presented in Figure 5.17, and they show that the additional CX events are not sufficient to equal the observed soft X-ray intensities. We find that the upper limit of CX emissions only increases the total soft X-ray intensity ~50%, which is not enough to account for the factors of three to six between the model and the observations. Furthermore, we stress

that the actual rate of sequential capture events present in these cometary systems is lower than this upper limit, so the actual emission intensities will reside between our model and the upper limit. We therefore find it unlikely that sequential CX events could account for these soft X-ray features.

As we are confident that both our CX model's resulting SW composition and photon yield emission rates are accurate, we therefore consider two possible explanations for the soft X-ray discrepancy:

1. Since the CX model does not match the observational intensities, it is possible we lack the SW ion type required to produce this feature. He^{2+} CX emissions, currently not included in our analysis, would be detectable in this soft X-ray region due to the low resolution of ACIS, and its high abundance may provide the required order-of-magnitude increase in intensity [21, 73]. Such SW ions would also have deeper penetration in the cometary atmosphere, which might also explain the collisionally thin appearance of the HRC morphology discussed in Section 4.1. Future iterations of our model should include this ion and compare the modified results to the soft X-ray emissions from ACIS.

2. The soft X-ray feature may be a result of previously undocumented detector contamination or degradation that sharply decays below 0.2 keV, producing a peak in observed spectrum. Examination of blank-sky observations taken at different stages of ACIS' lifetime would show if such a soft X-ray feature is always present or if this feature has manifested itself over time. If no emissions are detected in

this region for such observations, these features may therefore be cometary in origin.

The required analysis for each of these possibilities is beyond the scope of this research, but we believe that any future work on these soft X-ray features from ACIS should provide a thorough analysis of each possible explanation to determine the cause of these unique findings.

Chapter 6

Pluto Observations and Analysis

Similar to our discussion on cometary emissions, X-ray emissions from planetary systems are a well-studied phenomenon [1]. However, the study of planetary systems is complicated due to the introduction of auroral emissions from magnetosphere interactions with SW ions. These interactions bolster UV and X-ray emissions from the system, producing significant intensities that typically dwarf average CX and SF emissions [1]. In addition, auroral emissions can be fed via ions produced through thermalization in the upper atmosphere, making it difficult to properly determine the total SW ion contribution to the auroras. Planetary systems also possess dense atmospheres that we can no longer treat as optically thin, thereby relegating the majority of CX and SF emissions to the upper atmosphere, or exosphere, of the system. All of these complications mean our initial model is not valid for the majority of planetary systems and must be modified through the inclusion of magneto-hydrodynamics, thermalization, and internal scattering.

Instead of including these revisions, we may instead use our current model to analyze dwarf planetary systems. Dwarf planets, also known as planetesimals, are small

planet-like bodies that orbit the Sun, have sufficient self-gravity to achieve hydrostatic equilibrium, and are not satellites. These objects correspond to the middle point between the evolution of an asteroid to a planet. Due to the small size, dwarf planets normally have a diffuse atmosphere and limited tectonic activity. These conditions are perfect for analysis with our models as they strongly resemble those of a cometary system.

Of the dwarf planets available for observations, Pluto is the natural choice given the recent observations performed of it with the New Horizons probe. Although this probe did not have a X-ray spectrometer available, New Horizons provided valuable insight into SW conditions at Pluto as well as dust densities in its upper atmosphere that allow us to model its theoretical emission spectra. Recent results from New Horizons also confirmed that no auroral emissions were detected from Pluto, leaving only CX and SF as the primary X-ray emission mechanisms [74]. Pluto is also estimated to have a neutral particle loss rate similar to a comet at 1 AU, making it an excellent complement to our previous work. We therefore model the theoretical X-ray emissions from Pluto and compare our results to *Chandra* observations.

6.1 Pluto Observations

All X-ray observations of Pluto were performed with the *Chandra* ACIS-S instrument in very faint mode with the aimpoint on the S3 chip. These conditions are identical to previously analyzed comet observations. Further details on the observations are

Obs. Date	Obs. ID	$T_{\rm exp}$ (ks)	$r_{\rm P}$ (AU)	Δ (AU)	$V_{\rm P}$ (km s^{-1})
2014 Feb 24	15699	35.1	32.6	33.2	14.2
2015 Jul 26	17703	14.1	32.9	32.0	14.1
2015 Jul 30	17708	17.6	32.9	32.0	14.1
2015 Aug 01	17709	107.2	32.9	32.0	14.1

Table 6.1: Observation parameters are listed as follows: *Chandra* observation date, observation ID number, exposure time $T_{\rm exp}$, Pluto-Sun distance $r_{\rm P}$, Pluto-Earth distance Δ, and Pluto velocity $V_{\rm P}$.

listed in Table 6.1. We note that a preliminary observation was performed on Feb 24, 2014, while the New Horizons probe was 4 AU from its intersection with Pluto. The remaining observations were taken in conjunction with the New Horizons flyby. We therefore increase the uncertainty for our results of the initial observation as the SW conditions we will use for our model of Pluto are extracted from New Horizons.

Due to the significant distance between the detector and source object, the total count rate is significantly lower than what we find for an average cometary observation. We therefore cannot extract a emission spectrum due to the low counts. We instead isolate the energy range of each image to 0.3-2.0 keV and list the total counts detected within the 11×11 pixel source region set around Pluto. Results of this analysis are shown in Table 6.2. Adding the 4 observations together and accounting for background corrections, we find a total Pluto X-ray intensity of 6.79 ± 1.16 counts with a total

Obs. ID	Obs. Photon Energy (eV)	$V_{\rm SW}$ (km s^{-1})	$n_{\rm SW}$ (cm^{-3})
15699	597	364.67	0.01230
—	396	364.39	0.01249
17703	374	392.95	0.01016
17708	327	381.50	0.01286
17709	465	374.72	0.01399
—	405	375.39	0.01422
—	312	376.64	0.01096
—	477	376.95	0.00873

Table 6.2: Information on the observed Pluto photons. Observation parameters are listed as follows: *Chandra* observation proposal number, observed photon count energy, SW velocity $V_{\rm SW}$ and particle density $n_{\rm SW}$ detected at Pluto from New Horizons SWAP measurements.

count rate of $(3.9 \pm 0.7) \times 10^{-5}$ count sec^{-1}. Although these counts rates are small, the probability that such an observation would be due to the random background fluctuations would be as low as 5×10^{-4}. We therefore are confident that these observations are physical and, having excluded any background objects as the emission source, conclude that these emissions are coming from Pluto and, possibly, its moon Charon [75].

6.2 Modeling Pluto Emissions

As discussed in the previous sections, Pluto was selected for modeling as it shares similar properties to an average cometary system. We therefore do not have to modify our equations for Pluto and instead only adjust our variables accordingly. We also integrate our modeled spectra to calculate the total counts sec^{-1} as the low count rates from the observations make comparison to a spectrum impossible.

Through our anaylsis, we find that neither CX nor SF are satisfactory for emission rates detected from Pluto based on the following results:

- Coherent scattering is an unlikely source of the detected emissions as all observed photons were in the 0.33–0.06 keV energy range, while previous results from our cometary analysis show that scattering only dominates at energies greater than 1 keV. Results from our model agree with this theory as we return a count rate of 1.7×10^{-9} counts sec^{-1} for the 0.3–0.6 keV energy range, over three orders of magnitude lower than the observed emission rate. To match the observed intensity, a significant increase in either solar X-ray activity or scatterers would be required. However, extrapolation of measurements from the GOES X-ray sensor indicate that the Pluto observations were taken during a period of quiet solar X-ray activity. In addition, results from New Horizons provide significant constraints on the total dust densities present near Pluto and indicate such an increase in scatterers to be highly improbable [74].

- Initially, fluorescence appears to be a strong emission candidate since the observed composition signature agrees with fluorescence emissions from large concentrations of C, N, and O. All of these elements are present in high abundances in Pluto (high C and N) and its moon Charon (high H_2O). In addition, the ratio observed indicates a 5:1 C+N:O composition ratio, which agrees with the ∼4:1 ratio of Pluto:Charon's surface area [75]. However, our results show a total fluorescence count rate over the 0.3–0.6 keV range to be 6.2×10^{-8} counts sec^{-1}, three orders of magnitude lower than the observed rate. We note that the calculated fluorescence rate is entirely from the diffuse atmosphere in the system and does not include the possibility of surface-generated fluorescence, similar to X-ray emissions previously observed from the Moon [1]. Inclusion of surface-generated fluorescence would increase the results by 1–2 orders of magnitude, depending on the geometry of the observation. However, such results would demand Pluto's atmosphere to remain optically thin at all altitudes, and New Horizons' observations indicate a dense atmosphere at low altitudes [74]. We therefore conclude fluorescence to be unlikely, barring a massive shift in the understanding of Pluto's atmospheric density.

- CX emissions may be calculated to high accuracy given the New Horizons observations of SW conditions near Pluto. Using the physical parameters provided, we are able to calculate the total count rate for the 0.3–0.6 keV range as 2.1×10^{-6} count sec^{-1}, a factor of ∼20 lower than the observed intensity. Although

the value is closer than our previous calculations, the high precision in our SW inputs means that only an increase in neutral particle density could likely account for this discrepancy. In addition, simulated CX emissions normally demonstrate a C+N:O <1, while observations show a ratio ~5. Approximated SW composition ratios extrapolated from *ACE* indicate a C+N:O ratio closer to 0.5, even further from the observed ratio from Pluto. We do note that the observed ratio may be a by-product of the low count rate instead of a physical phenomenon, and further observations are recommended to provide improved statistics. Until then, we can only conclude that CX is unlikely to be the single emission source given the observational data provided.

Given these results, we are left with uncertainty over what the primary emission mechanism could be for Pluto. Scattering appears to be an insignificant mechanism, unless there is a significantly higher abundance of scatterers present than what is reported. Scattering may also be bolstered from an unreported resonance scattering cross section in the 0.3-0.6 keV range, which is unlikely. Fluorescence is also lower than the observed intensity, but the modeled results reproduce a similar spectral signature. Modeling of CX produces the highest emitted intensity and may equal the observed intensity given a slight increase in neutral particle density. The difference may indicate a dust tail-like structure trailing behind Pluto, similar to a comet, that would increase total neutral particles by a sizable fraction. In either case, the CX emissions would require a significant, and highly irregular, quenching of O ions in the SW before reaching Pluto

to be similar to the observed spectral composition signature. We therefore can only conclude that our current model is insufficient to accurately reproduce the observed Pluto X-ray spectrum and that further observations of Pluto, particularly regarding its diffuse density distributions, are required before accurate results may be derived.

Chapter 7

Conclusions

In summary, we developed a synthetic X-ray emission spectrum from a diffuse astrophysical atmosphere. Our model incorporates the three primary emission mechanisms for such a system:

1. Charge-exchange emissions from heavy, highly-ionized SW ions interacting with neutral particles in the atmosphere.

2. Coherent scattering of solar X-rays from gas and dust/ice particles, with a focus on nanoparticles. We also include approximations for total scattering contributions for dust grains of all sizes.

3. Fluorescence of neutral particles caused by excitation from solar X-rays.

Our work provides an updated CX emission model that includes large amounts of ion spectral lines induced in CX collisions and simplifies input variables while improving the physical accuracy in comparison to previous models. The SF component provides improved physical accuracy through the inclusion of dust/ice scatterers and is used

to determine the primary emission mechanism over the 0.3–2.0 keV range, whereas previous work has focused on analysis below 1.0 keV [5].

Using our model, we analyzed several comets of unique compositions and physical conditions. The observed X-ray morphologies from each comet was dramatically different, with comets IZ and ISON displaying an extended, well-developed X-ray coma. Average comets, like PanSTARRS, produced an unformed X-ray haze. Our morphological analysis indicates the markedly different SW conditions between the various observations, with ISON and IZ impacting an excited wind, while PanSTARRS traveled through fast SW.

Comparison of our CX model to observed spectra below 1.0 keV provided evidence of strong emissions induced in CX collisions of SW ions normally present within cometary emissions (C^{5+}, C^{6+}, N^{5+}, N^{6+}, N^{7+}, O^{6+}, O^{7+}, O^{8+}, Ne^{8+}, Ne^{9+}) from all observed comets. Analysis of IZ and ISON spectra showed higher concentrations of O^{8+} and Ne^{9+} due to above-average solar activity. Comet PanSTARRS demonstrated a more average CX spectra with higher O^{7+} concentration, indicating a lower SW ion freeze-in temperature during its observations.

Beyond CX analysis, we also examined total SF emissions present with cometary systems over the 0.3–2.0 keV energy range. Although we found SF to provide insignificant contributions at energies lower than 1.0 keV due to the abundance of CX emissions in this region, dust and ice scattering contributions were found to dominate in the 1.0–2.0 keV range. Due to poor signal-to-noise ratio at such energies, only two comets

in our analysis, IZ and ISON, showed any spectral peaks above 1.0 keV as both were observed during above average solar X-ray activity. We compared approximations of total dust scattering to both comets and found that IZ emissions matched our model in both intensity and spectral shape. Unfortunately, ISON did not agree with our model in intensity, which may indicate that dust density distributions within cometary atmospheres are highly dependent on unique physical constraints, such as jet-stream activity or comet surface area. Further observations of intense cometary X-ray emissions must be performed before a conclusion is reached as our current sample size is too small for definitive remarks.

In addition to our cometary analysis, we utilized our work to model X-rays emissions from the diffuse atmosphere of Pluto. Our analysis of each primary mechanism found that none fully replicated the observational data, with CX being closest in intensity and fluorescence being closest in spectral shape. These results may indicate the presence of dust tail behind Pluto that would increase the total neutral particles available for CX emissions. However, CX as the primary emissions mechanism would require an irregular quenching of O ions in the SW before reaching Pluto to match the observed SW composition. We therefore cannot provide conclusive evidence on the X-ray emission ratio from Pluto and advise additional observations of the object to determine if the current spectral shape is accurate or if it is a statistical anomaly.

Beyond successfully analyzing several objects, we also demonstrated our model's potential use as a SW ion composition analyzer. Our composition results agree well

with other SW composition tools available, such as *ACE*, while also calculating unique composition ratios not available through these other tools, like Ne^{8+}, Ne^{9+}, and Mg^{10+}. With further development of CX X-ray modeling, such an application would be possible for any CX emissions, not just those from comets. Our model also simplifies the variable inputs and provides an additional information on SW composition. We therefore intend to use such a model for all future CX analyses of cometary and planetary X-ray emissions as well as for investigations of CX X-rays induced in interaction between the SW plasma and interstellar gas.

In addition to our modeling results, we found the possibility of soft X-ray emissions around 0.2 keV detected from both comets ISON and PanSTARRS via ACIS. These soft X-ray features fluctuate similarly to those observed from the HRC observations and exceed the average spectral intensity uncertainty, leading us to believe these features to be cometary CX in origin. We extended our CX model to this soft X-ray region to compare, only to find our results lower in intensity than the observations by an order of magnitude. We also revise our model to include sequential CX capture events as these increase soft X-ray intensities, but we found that even the inclusion of more capture events is not sufficient to match the observed intensities. Based on our confidence in the model from its previous results, we believe this discrepancy to be a result of either a lack of SW ion types in the model that produce significant emissions in the soft X-ray region (such as He^{+}), detector contamination or degradation, or a combination of these possibilities. Investigations of these soft X-ray features should carefully explore

each explanation since confirmation of these features as physical emissions would open new opportunities in understanding cometary emission processes via *Chandra*.

Bibliography

[1] A. Bhardwaj, R. F. Elsner, G. R. Gladstone, T. E. Cravens, C. M. Lisse, K. Dennerl, G. Branduardi-Raymont, B. J. Wargelin, J. H. Waite Jr., I. Robertson, N. Østgaard, P. Beiersdorfer, S. L. Snowden, and V. Kharchenko. X-rays from solar system objects. *Planet. Space Sci.*, 55:1135, 2007.

[2] A. Fruscione, J. C. McDowell, G. E. Allen, N. S. Brickhouse, D. J. Burke, J. E. Davis, N. Durham, M. Elvis, E. C. Galle, D. E. Harris, D. P. Huenemoerder, J. C. Houck, B. Ishibashi, M. Karovska, F. Nicastro, M. S. Noble M. A. Nowak, F. A. Primini, A. Siemiginowska, R. K. Smith, and M. Wise. Ciao: Chandra's data analysis system. *Proc. SPIE*, 6270:62701V, 2006.

[3] B. Snios, V. Kharchenko, C. M. Lisse, S. J. Wolk, K. Dennerl, and M. R. Combi. Chandra observations of comets c/2012 s1 (ison) and c/2011 l4 (panstarrs). *ApJ*, 818(2):199, 2016.

[4] T. E. Cravens. Comet hyakutake x-ray source: Charge transfer of solar wind heavy ions. *Geophys. Res. Lett.*, 24:105, 1997.

[5] V. A. Krasnopolsky. On the nature of soft x-ray radiation in comets. *Icarus*, 128: 368, 1997.

[6] V. Kharchenko, M. Rigazio, A. Dalgarno, and V. A. Krasnopolsky. Charge abundances of the solar wind ions inferred from cometary x-ray spectra. *ApJ*, 585:L73, 2003.

[7] C. M. Lisse, T. E. Cravens, and K. Dennerl. X-ray and extreme ultraviolet emission from comets. In M. Festou, H. U. Keller, and H. A. Weaver, editors, *Comets II*, page 631. The University of Arizona Press, Tucson, 2004.

[8] D. Bodewits, D. J. Christian, M. Torney, M. Dryer, C. M. Lisse, K. Dennerl, T. H. Zurbuchen, S. J. Wolk, A. G. G. M. Tielens, and R. Hoekstra. Spectral analysis of the chandra comet survey. *A&A*, 469:1183, 2007.

[9] K. Dennerl. Charge transfer reactions. *Space Sci. Rev.*, 157(1-4):57–91, 2010.

[10] I. Ewing, D. J. Christian, D. Bodewits, K. Dennerl, C. M. Lisse, and S. J. Wolk. Emission lines between 1 and 2 kev in cometary x-ray spectra. *ApJ*, 763:66, 2013.

[11] M. F. A'Hearn, M. J. S. Belton, W. A. Delamere, L. M. Feaga, D. Hampton, J. Kissel, K. P. Klaasen, L. A. McFadden, K. J. Meech, H. J. Melosh, P. H. Schultz, J. M. Sunshine, P. C. Thomas, J. Veverka, D. D. Wellnitz, D. K. Yeomans, S. Besse, D. Bodewits, T. J. Bowling, B. T. Carcich, S. M. Collins, T. L. Farnham, O. Groussin, B. Hermalyn, M. S. Kelley, J. Li, D. J. Lindler, C. M. Lisse, S. A. McLaughlin, F. Merlin, S. Protopapa, J. E. Richardson, and J. L. Williams. Epoxi at comet hartley 2. *Science*, 332:1396, 2011.

[12] P. Bochsler. Minor ions in the solar wind. *A&A Rev.*, 14:1, 2007.

[13] D. Dijkkamp, Yu S. Gordeev, A. Brazuk, A. G. Drentje, and F. J. de Heer. Selective single-electron capture into (n, l) subshells in slow collisions of c^{6+}, n^{6+}, o^{6+} and ne^{6+} with he, h_2 and ar. *J. Phys. B*, 18(4):737, 1985.

[14] R. L. Kelly. Atomic and ionic spectrum lines below 2000 angstroms: Hydrogen through krypton, pt. 1. *J. Phys. Chem. Ref. Data*, 16(1):649, 1987.

[15] M. G. Suraud, R. Hoekstra, F. J. de Heer, J. J. Bonnet, and R. Morgenstern. State selective electron capture into nl subshells in slow collisions of c^{5+} and n^{6+} with he and h_2 studied by photon emission spectroscopy. *J. Phys. B*, 24(10):2543, 1991.

[16] W. L. Wiese, J. R. Fuhr, and T. M. Deters. *Atomic Transition Probabilities of Carbon, Nitrogen, and Oxygen: A Critical Data Compilation*. Am. Chem. Soc., Washington, DC, 1996.

[17] D. Koutroumpa, R. Lallement, V. Kharchenko, A. Dalgarno, R. Pepino, V. Izmodenov, and E. Quèmerais. Charge-transfer induced euv and soft x-ray emissions in the heliosphere. *A&A*, 460(1):289, 2006.

[18] D. Koutroumpa, R. Lallement, J. C. Raymond, and V. Kharchenko. The solar wind charge-transfer x-ray emission in the 1/4 kev energy range: Inferences on local bubble hot gas at low z. *ApJ*, 696(2):1517, 2009.

[19] A. Chutjian, J. Simcic, S. M. Madzunkov, J. A. MacAskill, R. J. Mawhorter, and E. Tsikata. Collision physics in the atomic and molecular universe. *JPCS*, 388 (1):012042, 2012.

[20] V. Kharchenko and A. Dalgarno. Spectra of cometary x rays induced by solar wind ions. *J. Geophys. Res*, 105(A8):18351–18359, 2000.

[21] V. Kharchenko and A. Dalgarno. Variability of cometary x-ray emission induced by solar wind ions. *ApJ*, 554(1):L99, 2001.

[22] V. A. Krasnopolsky, D. J. Christian, V. Kharchenko, A. Dalgarno, S. J. Wolk, C. M. Lisse, and S. A. Stern. X-ray emission from comet mcnaught-hartley (c/1999 t1). *Icarus*, 160(2):437–447, 2002.

[23] R. K. Janev and Hannspeter Winter. State-selective electron capture in atom-highly charged ion collisions. *Phys. Rep.*, 117(5-6):265–387, 1985.

[24] W. R. Johnson and G. Soff. The lamb shift in hydrogen-like atoms, 1 <z <110. *At. Data Nucl. Data Tab.*, 33(3):405–446, 1985.

[25] N. M. Cann and A. J. Thakkar. Oscillator strengths for *S* - *P* and *P-D* transitions in heliumlike ions. *Phys. Rev. A*, 46:5397–5405, 1992.

[26] R. K. Janev. *Atomic and Molecular Processes in Fusion Edge Plasmas*. Plenum, New York, 1995.

[27] C. Harel, H. Joiun, and B. Pons. Cross sections for electron capture from atomic hydrogen by fully stripped ions in the 0.051.00 a.u. impact velocity range. *At. Data. Nucl. Data Tables*, 68(2):279, 1998.

[28] J. Simcic, D. R. Schultz, R. J. Mawhorter, I. Čadež, J. B. Greenwood, A. Chutjian, C. M. Lisse, and S. J. Smith. Measurement and calculation of absolute single- and multiple-charge-exchange cross sections for fe^{q+} ions impacting co and co_2. *Phys. Rev. A*, 81:062715, 2010.

[29] A. Kramida, Yu. Ralchenko, J. Reader, and NIST ASD Team. Nist atomic spectra database (ver. 5.2), 2014.

[30] S. T. Lepri, E. Landi, and T. H. Zurbuchen. Solar wind heavy ions over solar cycle 23: Ace/swics measurements. *ApJ*, 768:94, 2013.

[31] V. A. Krasnopolsky, J. B. Greenwood, and P. C. Stancil. X-ray and extreme ultra-violet emissions from comets. *Space Sci. Rev.*, 113:271, 2004.

[32] R. von Steiger, N. A. Schwadron, L. A. Fisk, J. Geiss, G. Gloeckler, S. Hefti, B. Wilken, R. R. Wimmer-Schweingruber, and T. H. Zurbuchen. Composition of quasi-stationary solar wind flows from ulysses/solar wind ion composition spectrometer. *J. Geophys. Res*, 105:27217, 2000.

[33] W. M. Neupert. Variability of the solar soft x-ray irradiance (0.62.5 nm) with solar activity. *Adv. Space Res.*, 37:238, 2006.

[34] C. T. Chantler. Theoretical form factor, attenuation, and scattering tabulation for z=1–92 from e=1–10 ev to e=0.4–1.0 mev. *J. Phys. Chem. Ref. Data*, 24:71, 1995.

[35] M. J. Berger, J. H. Hubbell, S. M. Seltzer, J. Chang, J. S. Coursey, R. Sukumar, D. S. Zucker, and K. Olsen. Xcom: Photon cross section database (version 1.5). *[Online]*, 2010.

[36] B. M. McLaughlin, C. P. Ballance, K. P. Bowen, D. J. Gardenghi, and W. C. Stolte. High precision k-shell photoabsorption cross sections for atomic oxygen: Experiment and theory. *ApJ*, 771:L8, 2013.

[37] M. Rubin, V. M. Tenishev, M. R. Combi, K. C. Hansen, T. I. Gombosi, K. Altwegg, and H. Balsiger. Monte carlo modeling of neutral gas and dust in the coma of comet 1p/halley. *Icarus*, 213:655, 2011.

[38] U. Fink and M. Rubin. The calculation of afρ and mass loss rate for comets. *Icarus*, 221:721, 2012.

[39] B. T. Draine. Scattering by interstellar dust grains. ii. x-rays. *ApJ*, 598:1026, 2003.

[40] I. Mann. Interstellar dust in the solar system. *ARA&A*, 48:173, 2010.

[41] H. C. van de Hulst. *Light Scattering by Small Particles*. Courier Dover Publications, New York, 1981.

[42] M. I. Mishchenko, L. D. Travis, and A. A. Lacis. *Scattering, Absorption and Emission of Light by Small Particles*. Cambridge University Press, Cambridge, 2002.

[43] B. L. Henke, E. M. Gullikson, and J. C. Davis. X-ray interactions: Photoabsorption, scattering, transmission, and reflection at e = 50-30,000 ev, z = 1-92. *At. Data. Nucl. Data Tables*, 54:181, 1993.

[44] M. O. Krause. Atomic radiative and radiationless yields for k and l shells. *J. Phys. Chem. Ref. Data*, 8:307, 1979.

[45] B. Snios, N. Lewkow, and V. Kharchenko. Cometary emissions induced by scattering and fluorescence of solar x-rays. *A&A*, 568:A80, 2014.

[46] N. Biver, D. Bockelée-Morvan, J. Crovisier, D. C. Lis, R. Moreno, P. Colom, F. Henry, F. Herpin, G. Paubert, and M. Womack. Radio wavelength molecular observations of comets c/1999 t1 (mcnaught-hartley), c/2001 a2 (linear), c/2000 wm_1 (linear) and 153p/ikeya-zhang. *A&A*, 449:1255, 2006.

[47] C. M. Lisse, D. J. Christian, K. Dennerl, S. J. Wolk, D. Bodewits, R. Hoekstra, M. R. Combi, T. Mäkinen, M. Dryer, C. D. Fry, and H. Weaver. Chandra observations of comet 2p/encke 2003: First detection of a collisionally thin, fast solar wind charge exchange system. *ApJ*, 635:1329, 2005.

[48] D. J. Christian, D. Bodewits, C. M. Lisse, K. Dennerl, S. J. Wolk, H. Hsieh, T. H. Zurbuchen, and L. Zhao. Chandra observations of comets 8p/tuttle and 17p/holmes during solar minimum. *ApJS*, 187:447, 2010.

[49] N. G. Utterback and J. Kissel. Attogram dust cloud a million kilometers from comet halley. *AJ*, 100:1315, 1990.

[50] E. H. Beer, M. Podolak, and D. Prialnik. The contribution of icy grains to the activity of comets: I. grain lifetime and distribution. *Icarus*, 180:473, 2006.

[51] J. A. M. McDonnell, W. M. Alexander, W. M. Burton, E. Bussoletti, G. C. Evans S. T. Evans, J. G. Firth, R. J. L. Grard, S. F. Green, E. Grun, M. S. Hanner abd D. W. Hughes, E. Igenbergs, J. Kissel, H. Kuczera, B. A. Lindblad, Y. Langevin, J. C. Mandeville, S. Nappo, G. S. A. Pankiewicz, C. H. Perry, G. H. Schwehm, Z. Sekanina, T. J. Steveson, R. F. Turner, U. Weishaupt, M. K. Wallis, and J. C. Zarnecki. The dust distribution within the inner coma of come p/halley 1982i: Encoutner by giotto's impact detectors. *A&A*, 187:719, 1987.

[52] R. M. Häberli, T. I. Gombosi, D. L. De Zeeuw, M. R. Combi, and K. G. Powell. Modeling of cometary x-rays caused by solar wind minor ions. *Science*, 276:939, 1997.

[53] N. Fougere, M. R. Combi, M. Rubin, and V. Tenishev. Modeling the heterogeneous ice and gas coma of comet 103p/hartley 2. *Icarus*, 225:688, 2013.

[54] K. P. Dere, E. Landi, H. E. Mason, B. C. Monsignori Fossi, and P. R. Young. CHIANTI - an atomic database for emission lines. *A&AS*, 125:149, 1997.

[55] E. Landi, P. R. Young, K. P. Dere, G. Del Zanna, and H. E. Mason. Chianti atomic database for emission lines. xiii. soft x-ray improvements and other changes. *ApJ*, 763:86, 2013.

[56] D. L. McKenzie, P. B. Landecker, U. Feldman, and G. A. Doschek. The solar coronal x-ray spectrum from 5.5 to 12 å. *ApJ*, 289:849, 1985.

[57] C. M. Lisse, K. Dennerl, J. Englhauser, M. Harden, F. E. Marshall, M. J. Mumma, R. Petre, J. P. Pye, M. J. Ricketts, J. Schmitt, J. Trmper, and R. G. West. Discovery of x-ray and extreme ultraviolet emission from comet c/hyakutake 1996 b2. *Science*, 274(5285):205–209, 1996.

[58] R. Wegmann, K. Dennerl, and C. M. Lisse. The morphology of cometary x-ray emission. *A&A*, 428:647, 2004.

[59] R. Wegmann and K. Dennerl. X-ray tomography of a cometary bow shock. *A&A*, 430(2):L33, 2005.

[60] C. M. Lisse, D. J. Christian, S. J. Wolk, K. Dennerl, D. Bodewits, M. R. Combi, S. T. Lepri, T. H. Zurbuchen, J. Y. Li, N. Dello-Russo, M. J. S. Belton, and M. M. Knight. Chandra acis-s imaging spectroscopy of anomalously faint x-ray emission from comet 103p/hartley 2 during the {EPOXI} encounter. *Icarus*, 222(2):752, 2013.

[61] M. R. Combi, N. Fougere, J. T. T. Mäkinen, J.-L. Bertaux, E. Quémerais, and S. Ferron. Unusual water production activity of comet c/2012 s1 (ison): Outbursts and continuous fragmentation. *ApJ*, 788(1):L7, 2014.

[62] C. M. Lisse, D. J. Christian, K. Dennerl, K. J. Meech, R. Petre, H. A. Weaver, and S. J. Wolk. Charge exchange-induced x-ray emission from comet c/1999 s4 (linear). *Science*, 292:1343, 2001.

[63] M. R. Combi, J.-L. Bertaux, E. Quémerais, S. Ferron, J. T. T. Mäkinen, and G. Aptekar. Water production in comets c/2011 l4 (panstarrs) and c/2012 f6 (lemmon) from observations with soho/swan. *ApJ*, 147(6):126, 2014.

[64] G. Branduardi-Raymont, A. Bhardwaj, R. F. Elsner, G. R. Gladstone, G. Ramsay, P. Rodriguez, R. Soria, J. H. Waite Jr., and T. E. Cravens. Latest results on jovian disk x-rays from xmm-newton. *Planet. Space Sci.*, 55:1126, 2007.

[65] G. Branduardi-Raymont, R. F. Elsner, M. Galand, D. Grodent, T. E. Cravens, P. Ford, G. R. Gladstone, and J. H. Waite. Spectral morphology of the x-ray emission from jupiter's aurorae. *J. Geophys. Res: Space Physics*, 113, 2008.

[66] M. R. Combi, J. T. T. Mäkinen, J. L. Bertaux, E. Quémerais, S. Ferron, and N. Fougere. Water production rate of comet c/2009 p1 (garradd) throughout the 2011–2012 apparition: Evidence for an icy grain halo. *Icarus*, 225:740, 2013.

[67] M. de Val-Borro, D. Bockelée-Morvan, E. Jehin, P. Hartogh, C. Opitom, S. Szutowicz, N. Biver, J. Crovisier, D. C. Lis, L. Rezac, Th. de Graauw, D. Hutsemékers, C. Jarchow, M. Kidger, M. Küppers, L. M. Lara, J. Manfroid, M. Rengel, B. M. Swinyard, D. Teyssier, B. Vandenbussche, and C. Waelkens. Herschel observations of gas and dust in comet c/2006 w3 (christensen) at 5 au from the sun. *A&A*, 564:A124, 2014.

[68] Y. Shen, B. T. Draine, and E. T. Johnson. Modeling porous dust grains with ballistic aggregates. i. geometry and optical properties. *ApJ*, 689:260, 2008.

[69] B. Yang, J. Keane, K. Meech, T. Owen, and R. Wainscoat. Multi-wavelength observation of comet c/2011 l4 (pan-starrs). *ApJL*, 784:L23, 2014.

[70] N. Djurić, J. A. Lozano, S. J. Smith, and A. Chutjian. Surface charging and x-ray emission from insulator surfaces induced by collisions with highly charged ions: Relevance to cometary and planetary spectroscopy. *ApJ*, 635(1):718, 2005.

[71] S. J. Wolk, C. M. Lisse, D. Bodewits, D. J. Christian, and K. Dennerl. Chandra's close encounter with the disintegrating comets 73p/2006 (schwassmann-wachmann 3) fragment b and c/1999 s4 (linear). *ApJ*, 694(2):1293, 2009.

[72] J. Lichtman, B. Snios, and V. Kharchenko. Universality of cometary x-ray emissions. *ApJL*, in prep.

[73] D. Bodewits, R. W. McCullough, A. G. G. M. Tielens, and R. Hoekstra. X-ray and far-ultraviolet emission from comets: Relevant charge exchange processes. *Physica Scripta*, 70(6):C17, 2004.

[74] G. R. Gladstone, S. A. Stern, K. Ennico, C. B. Olkin, H. A. Weaver, L. A. Young, M. E. Summers, D. F. Strobel, D. P. Hinson, J. A. Kammer, A. H. Parker, A. J. Steffl, I. D. Linscott, J. Wm. Parker, A. F. Cheng, D. C. Slater, M. H. Versteeg, T. K. Greathouse, K. D. Retherford, H. Throop, N. J. Cunningham, W. W. Woods, K. N. Singer, C. C. C. Tsang, E. Schindhelm, C. M. Lisse, M. L. Wong, Y. L. Yung, X. Zhu, W. Curdt, P. Lavvas, E. F. Young, G. L. Tyler, and New Horizons Team. The atmosphere of pluto as observed by new horizons. *Science*, 351(6279), 2016.

[75] C. M. Lisse, R. L. McNutt Jr., S. J. Wolk, F. Bagenal, S. A. Stern, G. R. Gladstone, T. E. Cravens, M. E. Hill, P. Kollmann, H. A. Weaver, D. F. Strobel, H. A. Elliot, D. J. McComas, R. P. Binzel, B. T. Snios, A. Bhardwaj, A. Chutjian, L. A. Young, C. B. Olkin, and K. A. Ennico. The puzzling detection of x-rays from pluto by chandra. *Icarus*, submitted.

Appendix A

Emission Model Code Repository

All emission spectra modeling discussed in this work is written in C++ and is openly available for free use and modification. Links for all programs can be found in the following repository:

http://github.com/astropsychics